**Title**
Plasmon-Enhanced Monolayer MoS2 for Efficient and Sustainable Photocatalytic Water Splitting Platform



**Author**
Ye, Peiyi

**Publication Date**
2020

Peer reviewed|Thesis/dissertation

UNIVERISTY OF CALIFORNIA

Los Angeles

# Plasmon-Enhanced Monolayer $MoS_2$ for Efficient and Sustainable Photocatalytic Water Splitting Platform

A dissertation submitted in partial satisfaction of the

requirements for the degree Doctor of Philosophy

in Materials Science and Engineering

by

Peiyi Ye

2020

ABSTRACT OF THE DISSERTATION

Plasmon-Enhanced Monolayer $MoS_2$ for Efficient and Sustainable Photocatalytic Water Splitting Platform

by

Peiyi Ye

Doctor of Philosophy in Materials Science and Engineering

University of California, Los Angeles, 2020

Professor Ya-Hong Xie, Chair

$H_2$ has long been known to be one of the highest energy density fuels. Fuel cell technology has been actively pursued as an environmentally friendly power source for automobiles. The promise of the technology is hindered by the lacking of a sustainable way of producing $H_2$. Solar water-splitting via photo-electrochemical cells (PEC) is the most promising approach which converts the sustainable solar energy to the chemical energy store inside the $H_2$ bonding. The materials that can be used in a PEC cell must fulfil a variety of thermodynamic and kinetic requirements to ensure good efficiency and durability. Single-layer $MoS_2$ possess the corrected energy bandgap of 1.9 eV which allows for sufficient over-potential while still being capable of absorbing the majority of the solar spectrum. However, the limited optical absorbance from single-layer $MoS_2$ prevent it from widely used. This shortcoming of the single-layer thickness of $MoS_2$ is overcome by superimposing the $MoS_2$ with plasmonic surface that serves to

amplify the enhanced electromagnetic field where the $MoS_2$ is located, allowing single-layer $MoS_2$ to efficiently absorb Sun light thus producing $H_2$.

In the first part of dissertation, a novel two-step chemical vapor deposition method is developed to consistently grow high coverage and exclusive single-layer $MoS_2$. Up to 90% surface coverage and single-layer $MoS_2$ is successfully fabricated. This is a crucial step to conduct the follow-up experiments.

In the second part of dissertation, A facile one-pot synthetic approach for synthesis hollow Au nanoframes structure is reported for the first time. A growth mechanism has been revealed that involves a synergistic function of Ag and Br ions. The presence of $Ag^+$ lead to observed self-limiting of Au film thickness whereas Au {111} facets are preferentially attacked by the presence of $Br^-$ in the reaction ambient. Combined simulation and experimental studies show strong plasmonic effect that the hybrid platform made of graphene/Au nanoframes is capable of detecting analytes at concentration levels down to $10^{-9}$ M by using the surface-enhanced Raman spectroscopy (SERS) technique.

In the last part of the dissertation, the plasmonic effect generated from nano-structured metal surfaces is introduced to offset the small thickness from single-layer $MoS_2$ and improve the overall absorption. It is demonstrated for the first time that using single-layer $MoS_2$ as a well-defined nanospacer between Au-nanoparticles and Au-film (gap plasmon system). The field enhancement is known to be inversely proportional to this gap thickness. Hence reducing the gap thickness is important to achieve the highest possible field enhancement. In this work, it is demonstrated for the first time that using

single-layer $MoS_2$ as a well-defined nanospacer between Au-nanoparticles (AuNPs) and Au-film, which could offer an extremely high localized electric field enhancement within the gap. The $MoS_2$ Raman intensity with the Surface Enhanced Raman Scattering (SERS) enhancement factor (EF) up to $5x10^6$ is obtained from the $MoS_2$-Au gap plasmon system. A 5-fold increase in the photocurrent is obtained from the $MoS_2$-Au gap plasmon as the working electrode compared to that from bare $MoS_2$ prepared under the same condition. Compared with individual metal nanoparticles commonly used to enhance thin-film photocatalytic process, gap-plasmon could theoretically produce 8 orders of magnitude higher SERS EF and precise control the hot spot location to superimpose where ultrathin materials locate thus using the higher incident energy available.

The dissertation of Peiyi Ye is approved.

Ali Mosleh

Dwight Streit

Xiaochun Li

Ya-Hong Xie, Committee Chair

University of California, Los Angeles

2020

Dedicated to my family, teachers and friends

TABLE OF CONTENTS

LIST OF FIGURES

ACKNOWLEDGEMENTS

I would like to deliver my sincere gratitude to my supervisor Professor Ya-Hong Xie, who has offered me priceless guidance during my Ph.D study at UCLA. Under Prof. Xie's mentorship, I not only learned how to conducted research independently, but also developed my skills on critical thinking. I also want to acknowledge my committee members Professor Dwight Streit, Professor Ali Mosleh and Professor Xiaochun Li who have inspired me to construct scientific sense and motivated me to be an independent scientist.

I would also like to thank my former and my current lab members and colleagues. I have benefited a lot from the collaboration with them. Dr. Wei Zhang, Dr. Ming Xia, Dr. Zhongbo Yan, Dr. Xinke Yu, Dr. Jimmy Ng, Zirui Liu, Owen Liang, Shan Huang, Jun Liu. I would also like to thank Professor Suneel Kodambaka for sharing his lab with me to fulfil my experiment plan. I want to thank my collaborators during my PhD research. I want thank Dr. Wenbo Xin for teaching me the knowledge of assembling controllable shape of gold nanocrystals. I also want to thank Prof Li Zheng from Shanghai Institute of Microsystem and Information Technology who provide me with some necessary experiment support.

Finally, I would like to thank my family. My special thank goes to my wife, Menglu Li, my daughter Lori Ye who has been accompanying me throughout all the years of my Ph.D study. My parents, Baobin Ye and Jun Zhao, who have been always supportive.

# VITA

2008-2012 Department of Materials Science and Engineering,

Shanghai Jiaotong University, China

2012-2013 Department of Materials Science and Engineering

University of California Berkeley, USA

2013-2020 Department of Materials Science and Engineering,

University of California, Los Angeles, USA

# Chapter 1 Introduction

## 1.1 Motivation of the thesis

$H_2$ has long been known to be one of the highest energy density fuels[1]. Fuel cell technology has been actively pursued as an environmentally friendly power source for automobiles[2]. The promise of the technology is hindered by the lacking of a sustainable way of producing $H_2$. Solar water-splitting via photo-electrochemical cells (PEC)[3] is the most promising approach with intense research effort being dedicated to it. To date, only a handful of semiconductor materials meet these stringent requirements such as GaP[4], $TiO_2$[5-7] and $MoS_2$[8-10]. Among them, single-layer $MoS_2$ possesses the largest chemical over-potential[8-9] with films thicker than a one-molecular layer having energy bandgap values too small for the intended purpose. $MoS_2$ is one member of the family of "van der Waals materials" (vdW), named after the nature of van der Waals bonding in between layers. The requirement of a one-molecular layer thickness makes the use of $MoS_2$ impractical because of the limited absorption of sunlight by the extremely thin film. Consequently, Most of the research efforts on solar water-splitting have been directed at using tandem semiconductor junctions with their own set of technological challenges that are yet to be overcome[11-12]. The thesis addresses the major roadblock that preventing the use of a single-layer $MoS_2$ for solar water-splitting by adapting surface plasmon resonance (SPR), a phenomenon of collective oscillation of conducting electrons at nanostructured metal surfaces when excited by light[13]. The primary shortcoming of the single molecular-layer thickness of $MoS_2$ is overcome by superimposing the $MoS_2$ over a plasmonic surface that serves to amplify the electromagnetic field where the $MoS_2$ locates, allowing single-layer $MoS_2$ to

efficiently absorb sunlight thus producing $H_2$. This $MoS_2$ coupled plasmonic platform proves the much higher $H_2$ production, which help significant reduction in greenhouse gas emissions. It is an important and ingenious utilization of van der Waals materials and Plasmon resonance while chartering out the pathway for them to enter commercial-scale production.

This chapter introduces the background information, the properties and the common methods to grow transition metal dichalcogenide is introduced in section 1.2, the principle of surface plasmon resonance in section 1.3, the principle of the photo-electrochemical water-splitting platform is introduced in section 1.4, the outline of the thesis is lastly introduced in section 1.5.

## 1.2 Transition Metal Dichalcogenides

The transition metal dichalcogenides (TMDs) are one type of van der Waals materials that contain one transition metal center (Mo, W) and six surrounded chalcogenide atoms (S, Se, Te) that sandwiching the transition metal atoms[14] (Figure 1.1a). Among them, the most famous and widely studied TMD materials belong to $MoS_2$, it is a silvery black solid that naturally occurs as the mineral molybdenite[15]. It is widely utilized as an industrial lubricant due to its weak van der Waals interactions between layers, it is also relatively unreactive, unaffected by dilute acids and $O_2$[16]. $MoS_2$ usually consists of a mixture of two major polytypes, with the 2-H form being more abundant, in 2-H crystal structure with a P63/mmc point group (Figure 1.1 b, c)[14, 17]. In 2-H form $MoS_2$ unit cell, each Mo center occupies a trigonal prismatic coordination sphere and is bound to six S, each S center is

pyramidal and is connected with 3 Mo.

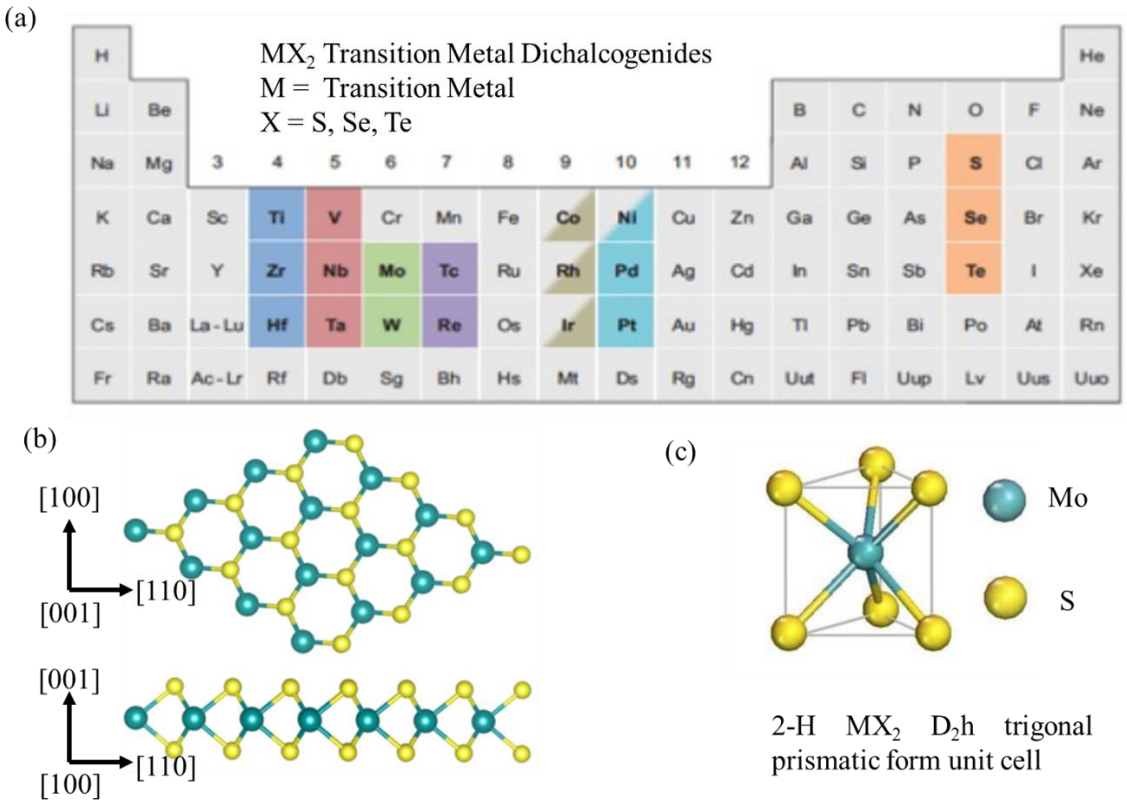


Figure 1. 1 (a) Periodic table highlighting element available for the transition metals and chalcogenides, (b) Crystal structure of group 6 transition metal dichalcogenides; 2-H hexagonal trigonal prismatic crystal structure. A single layer is consisting of a chalcogen sandwiching a metal atom. (c) $D_3h$ trigonal unit cell. Images adapted from reference[17]

The electronic properties of bulk $MoS_2$ is semiconducting with a 1.2 eV indirect band gap[18]. There is a considerable energy band shift from an indirect-to-direct band gap that is typically found within all group six TMD materials, the $MoS_2$ band structure shift while changing from bulk form to single-layer form can be seen in Figure 1.2. When the layer number gradually decreases till the separated two-dimension sheet, the energy of the valence bands decreases due to the antibonding feature of that orbital interactions[19]. On the other hand, the maximum of the valence band and the minimum of the conduction band do not change when the layers detach at the K-point. The energy states at the K-point consist of Mo-Mo $d_{xy}$ and $d_{dx^2-y^2}$ exchanges, within the plane of the $MoS_2$ and it is independent of interlayer distance[19]. The gap between these two energy levels keeps constant around 1.9 eV and doesn't require momentum change[19]. In this case, when $MoS_2$ layer decrease to a single layer, there is a noticeable electronic structure shift from a 1.2 eV indirect band gap ($\Gamma \rightarrow K$) to a 1.9 eV direct band gap ($K \rightarrow K$).

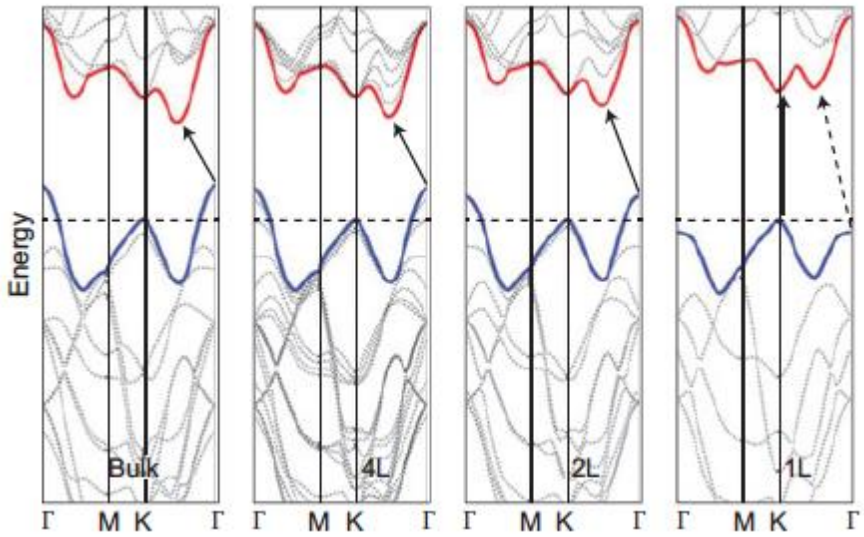


Figure 1. 2 Energy band diagram in bulk, 4L, 2L and monolayer MoS2. The electronic signature shift from indirect to direct when thickness reaches to a monolayer. Image adapted from reference[20].

Chemical vapor deposition (CVD) is an easy and most widely adapted bottom-up methods to grow two-dimension materials[21]. Starting from 2012, a lot of new CVD methods have been reported to grow single-layer $MoS_2$. Atomically thin Mo film was deposited on a substrate followed by S annealing to form layer $MoS_2$ was reported[15]. Follow a similar procedure, $MoO_3$ was used as Mo precursor to deposited on a substrate followed by annealing sulfur vapor at a high temperature[22]. Another Mo precursor was also introduced by using $(NH_4)_2MoS_4$ solution on a substrate, followed by sulfur vapor annealing vapor[23]. From another paper, $MoO_3$ was first evaporated to form a $MoO_2$ template followed by treatment with sulfur vapor[24]. All of these methods above reports have two major drawbacks: first, the non-uniform $MoS_2$ thickness distribution along the substrate, second, the non-continuous $MoS_2$ film growth on the substrate. The performance

of electric and optoelectronic is significantly hindered by those drawbacks. In the second chapter of the dissertation a novel method to grow near continuously exclusive single-layer $MoS_2$ is introduced that can be used as in a wider application including the photoelectrochemical cells in water splitting application that is described in Chapter 4.

## 1.3 Surface Plasmonic Resonance

Surface plasmon resonance (SPR) is a resonant oscillation of conduction electrons at the interface between materials of negative and positive dielectric constants excited via incident light. SPR was first discovered by Kretschmann and Raether [25]. Since then, intensive attention has been paid to this field, the principles and related application can be found in numerous papers, for example, SPR principles from Davis, L.C. et al. at 1977[26], SPR sensors from J. Homola. et al[27-29] , Surface-enhanced Raman scattering from A. Campion et al[30].

In general. there are two different types of surface plasmons, depending on the geometry of the metals shown in Figure 1.3a, the schematic of SPR on the interface between the thin metal film and a dielectric as well as on individual nanoparticles. SPR together with a metallic thin film of thickness can travel along the interface, which is called propagating SPR or surface plasmon polariton(SPP)[31]. The SPR associated with metal nanoparticles with the size between 10 to 200 nm is localized to the neighboring metal nanoparticle, which is named localized SPR (LSPR)[32], schematically shown in Figure 1.3b.

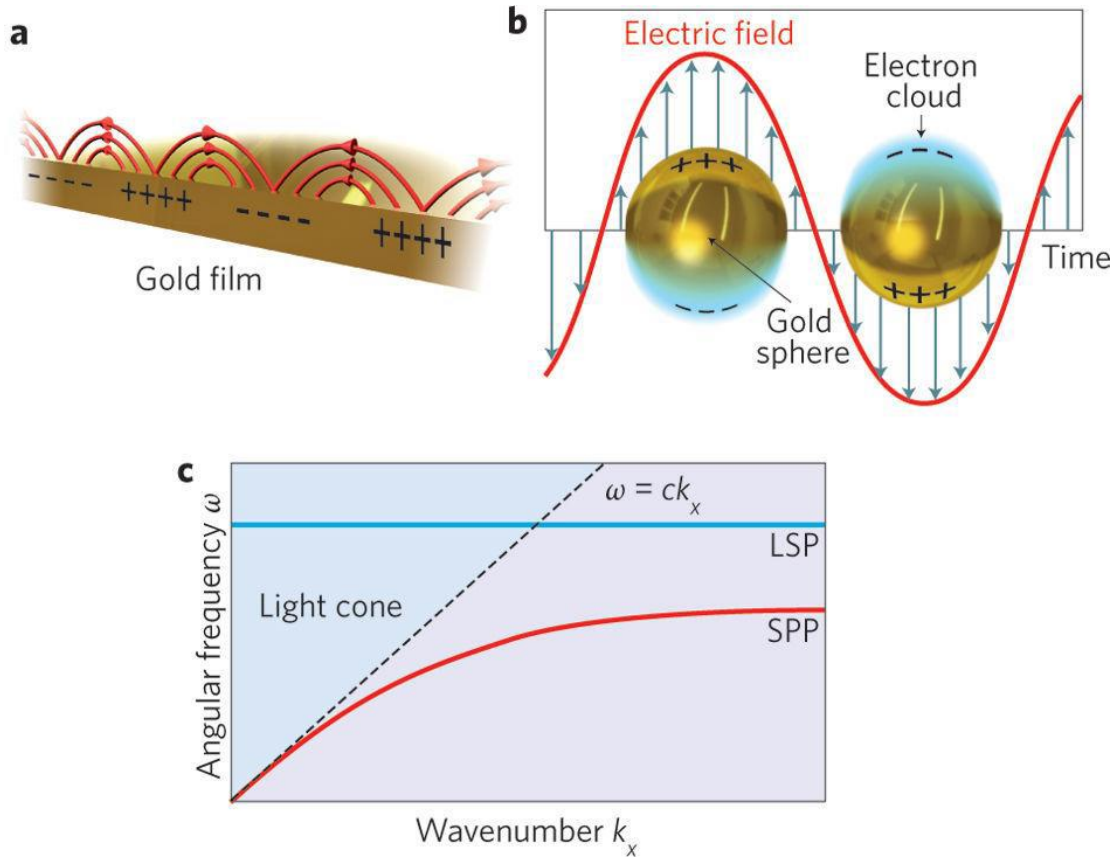


Figure 1. 3 (a) Illustration of surface plasmon polariton (SPP) (b) Illustration of localized surface plasmon resonance (LSPR). (c) Typical dispersion curves of SPPs (red) and LSPs (blue) Adapted from reference[33]

LSPR is the collective electron charge oscillations within individual metal nanoparticles. They show enhanced near-field electromagnetic fields at the resonance frequency. This enhanced field is highly localized near the surface of metal nanoparticles which decreased rapidly away from the surface into the dielectric surrounding environment. The LSPR has a very high spatial resolution (subwavelength) due to the localization, limited only by the size of nanoparticles. SPPs have a continuous dispersion relation thus

exists over a long range of frequency, however, LSPR only exists on a limited frequency range due to the additional constraints limited via its finite dimensions shown in Figure 1.3c. The particle's shape, size as well as dielectric functions of both the metal and the surrounding media are major parameters that control the spectral position of the SPR. Furthermore, SPPs cannot be directly coupled with propagating light while SPRs could.

A variety of metals, including commonly used gold, silver as well as some not commonly used copper, aluminum, sodium, indium, titanium, and chromium, can show SPR[34]. Compared with nanostructures made from other uncommon materials, gold and silver have been paid much more attention due to their unique optical properties. As shown in Figure 1.4, silver and gold nanostructures exhibit a wide range high quality factor or Q factor which is a dimensionless parameter that represents how underdamped a resonator is along the wavelength. In another word, Au and Ag SPR can be more easily for broadband resonant compared with other metal candidates. It is worth to mention that silver is too easy to oxidation in the air and most of the time it could be poisonous to biological samples, so usually gold is preferred for bio-sensing or used in a harsh environment. Recently, A wide range of applications have been realized via using plasmonic, such as high-resolution optical imaging below the diffraction limit, bio-detection at single-molecule level, surface-enhanced Raman scattering, enhanced optical transmission through sub-wavelength apertures, etc. Undoubtedly, there will be more and more findings and new applications in the field of surface plasmon resonance in the near future.

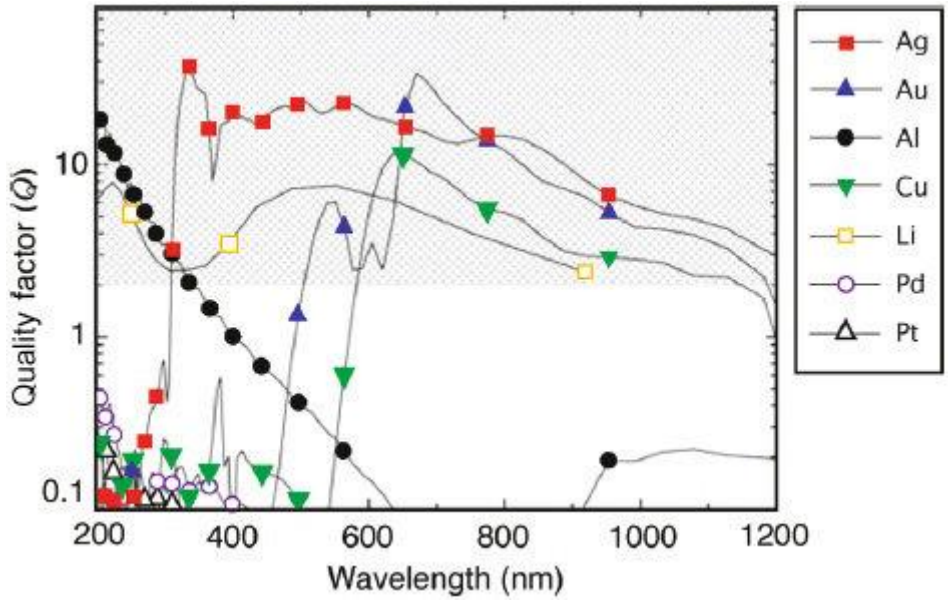


Figure 1. 4 Quality factor (Q) of localized surface plasmon resonance between metal and air. Adapted from reference[34]

## 1.4 Photoelectrochemical Water Splitting

A lot of previously published books[35-37] and review articles[38-39] have already discussed the very detailed working principles of PEC cell. However, the basic operation principle of the PEC cell is worth to introduce briefly here. The schematic in figure 1.5 showed a typical PEC cell with a two-electrode system, one electrode we called working electrode, which using an n-type semiconductor as photoanode. Incoming photons excite the semiconductor to generate electrons and holes pairs. The photogenerated electrons and holes pairs separate and move through the semiconductor in opposite directions; The holes participate the oxygen evolution reaction (OER) at the surface of the photoanode or working electrode. At the same time, the electrons are diffused towards the surface of the

counter electrode or counter electrode to participate the hydrogen evolution reaction (HER). It is also shown the minimum thermodynamic energy required for splitting water is 1.23 ev in Figure 1.5. A little overpotential is required to drive the kinetics of the HER and OER at the interface between solid and liquid. Minimizing these overpotentials is the key step to get the efficient catalysts for making highly efficient water splitting devices. Among all the available semiconductor, single-layer $MoS_2$ stands out as a great candidate for solar water-splitting. In addition to its corrosion resistance, single-layer $MoS_2$ is a direct bandgap semiconductor with ideal energy band structures: The conduction band edge (CB) is above that of the $H^+/H_2$ reduction of $H^+$ in water, and the valence band edge (VB) is below that of $H_2O/O_2$ potential[20]. The energy bandgap ($E_g$) of 1.9eV allows for sufficient over-potential for $H_2$ production (1.23 eV)[40] while still being capable of absorbing almost all of the solar spectrum. The nature of direct bandgap means large oscillator strengths for electron-photon interaction and high quantum efficiency. The details on $MoS_2$-based photoelectrochemical water splitting is studied in Chapter 4.

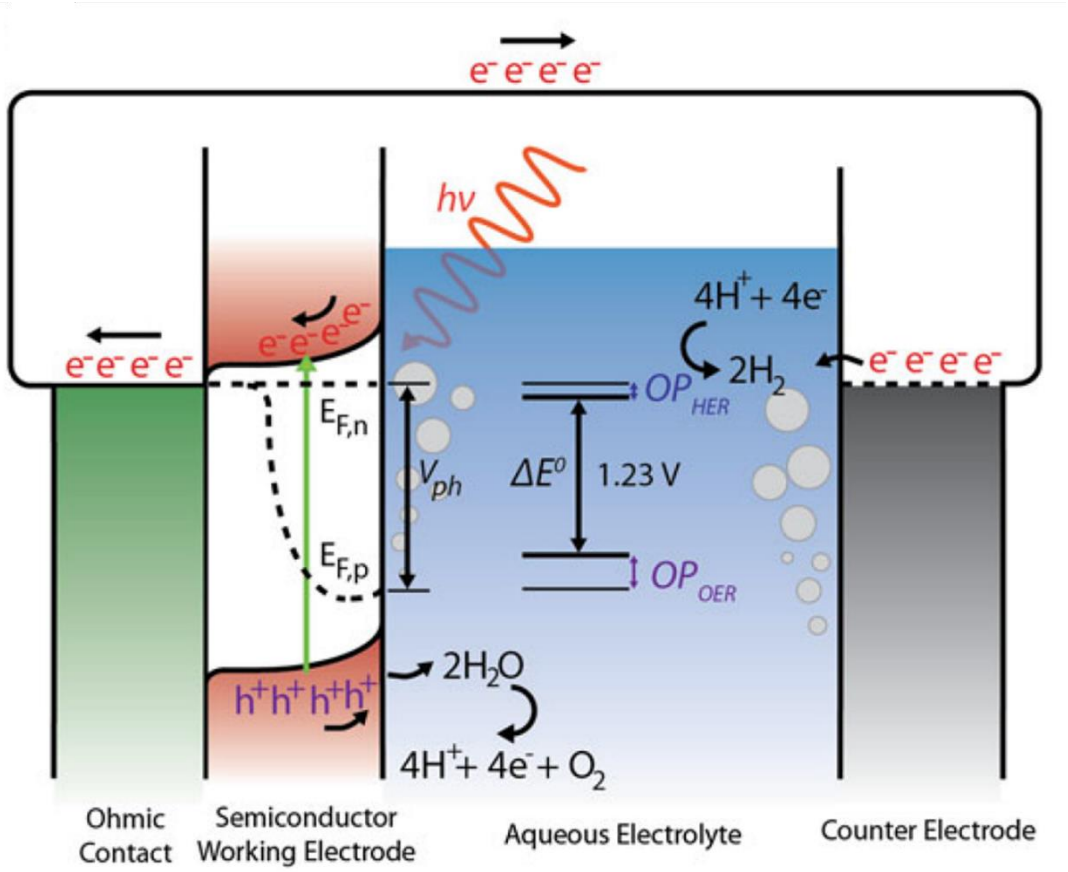


Figure 1. 5 Schematic and Band structure of an n-type semiconductor as photoanode within water splitting device. The processes include photon irradiation, electron–hole pair formation, charge transport, and interfacial reactions. Adapted from reference[41]

## 1.5 Outline of the Thesis

Chapter 1 introduces the motivations of the thesis, basic principle and typical growth method for transitional metal dichalcogenides $MoS_2$, the basic principle of surface plasmon resonance and photo-electrochemical water splitting platform.

Chapter 2 introduces a novel and controlled two-step method to grow $MoS_2$ on carbon nanotube (CNT) substrate via typical chemical vapor deposition (CVD)[42] setup, the growth method is significant in the following two aspects: first, direct growth of large quantity $MoS_2$ nanoflakes on carbon nanotube sheet is realized for the first time; second, plasma activated CNT sheet is of critical importance to immobilize $MoS_2$ nanoflakes. We reveal that plasma treatment of CNT sheet results in de-bundling and activation of carbon nanotube bundles, which promotes the deposition of $MoS_2$ nanoflakes.

Chapter 3 presents a novel method for synthesizing well-defined Au nanoframes with tunable size on graphene substrate, which shows an extremely strong surface plasmon resonances via simulation and experimental study. A comprehensive investigation on structures and morphologies of graphene-Au nanoframes is studied to improve the electric field and the overall electric field enhancement nearby. A similar method is used for synthesizing Au nanoparticles for the solar water splitting application in Chapter 4

Chapter 4 demonstrates the feasibility by using single-layer $MoS_2$ over a plasmonic surface for efficient water splitting applications. The primary shortcoming of the single molecular-layer thickness of $MoS_2$ is overcome by superimposing the $MoS_2$ over the

plasmonic surface that serves to amplify the electromagnetic field where the $MoS_2$ locates, allowing single-layer $MoS_2$ to efficiently absorb Sunlight thus producing $H_2$.

Chapter 5 concludes the dissertation by providing each chapter's results with a section that proposes future work that can build on the results presented herein.

1.6 References


1. Veziroğlu, T. N., Hydrogen movement and the next action: fossil fuels industry and sustainability economics. *International journal of hydrogen energy* 1997, *22* (6), 551-556.

2. O'hayre, R.; Cha, S.-W.; Colella, W.; Prinz, F. B., *Fuel cell fundamentals*. John Wiley & Sons: 2016.

3. Grätzel, M., Photoelectrochemical cells. *nature* 2001, *414* (6861), 338-344.

4. Mettee, H.; Otvos, J. W.; Calvin, M., Solar induced water splitting with p/n heterotype photochemical diodes: n-Fe2O3/p-GaP. *Solar Energy Materials* 1981, *4* (4), 443-453.

5. Wang, G.; Wang, H.; Ling, Y.; Tang, Y.; Yang, X.; Fitzmorris, R. C.; Wang, C.; Zhang, J. Z.; Li, Y., Hydrogen-treated TiO2 nanowire arrays for photoelectrochemical water splitting. *Nano letters* 2011, *11* (7), 3026-3033.

6. Ni, M.; Leung, M. K.; Leung, D. Y.; Sumathy, K., A review and recent developments in photocatalytic water-splitting using TiO2 for hydrogen production. *Renewable and Sustainable Energy Reviews* 2007, *11* (3), 401-425.

7. Khan, S. U.; Al-Shahry, M.; Ingler, W. B., Efficient photochemical water splitting by a chemically modified n-TiO2. *science* 2002, *297* (5590), 2243-2245.

8. Yin, Z.; Chen, B.; Bosman, M.; Cao, X.; Chen, J.; Zheng, B.; Zhang, H., Au nanoparticle-modified MoS2 nanosheet-based photoelectrochemical cells for water splitting. *Small* 2014, *10* (17), 3537-3543.

9. Joshi, R.; Shukla, S.; Saxena, S.; Lee, G.-H.; Sahajwalla, V.; Alwarappan, S., Hydrogen generation via photoelectrochemical water splitting using chemically exfoliated MoS2 layers. *AIP Advances* 2016, *6* (1), 015315.

10. Huang, Z.; Han, W.; Tang, H.; Ren, L.; Chander, D. S.; Qi, X.; Zhang, H., Photoelectrochemical-type sunlight photodetector based on MoS2/graphene heterostructure. *2D Materials* 2015, *2* (3), 035011.

11. Walter, M. G.; Warren, E. L.; McKone, J. R.; Boettcher, S. W.; Mi, Q.; Santori, E. A.; Lewis, N. S., Solar water splitting cells. *Chemical reviews* 2010, *110* (11), 6446-6473.

12. Brillet, J.; Yum, J.-H.; Cornuz, M.; Hisatomi, T.; Solarska, R.; Augustynski, J.; Graetzel, M.; Sivula, K., Highly efficient water splitting by a dual-absorber tandem cell. *Nature Photonics* 2012, *6* (12), 824-828.

13. Ritchie, R. H., Plasma losses by fast electrons in thin films. *Physical review* 1957, *106* (5), 874.

14. Manzeli, S.; Ovchinnikov, D.; Pasquier, D.; Yazyev, O. V.; Kis, A., 2D transition metal dichalcogenides. *Nature Reviews Materials* 2017, *2* (8), 17033.

15. Zhan, Y.; Liu, Z.; Najmaei, S.; Ajayan, P. M.; Lou, J., Large-Area Vapor-Phase Growth and Characterization of MoS2 Atomic Layers on a SiO2 Substrate. *Small* 2012, *8* (7), 966-971.

16. Li, H.; Zhang, Q.; Yap, C. C. R.; Tay, B. K.; Edwin, T. H. T.; Olivier, A.; Baillargeat, D., From bulk to monolayer MoS2: evolution of Raman scattering. *Advanced Functional Materials* 2012, *22* (7), 1385-1390.

17. Chhowalla, M.; Shin, H. S.; Eda, G.; Li, L.-J.; Loh, K. P.; Zhang, H., The chemistry of two-dimensional layered transition metal dichalcogenide nanosheets. *Nature chemistry* 2013, *5* (4), 263.

18. Kam, K.; Parkinson, B., Detailed photocurrent spectroscopy of the semiconducting group VIB transition metal dichalcogenides. *The Journal of Physical Chemistry* 1982, *86* (4), 463-467.

19. Li, T.; Galli, G., Electronic properties of MoS2 nanoparticles. *The Journal of Physical Chemistry C* 2007, *111* (44), 16192-16196.

20. Kang, J.; Tongay, S.; Zhou, J.; Li, J.; Wu, J., Band offsets and heterostructures of two-dimensional semiconductors. *Applied Physics Letters* 2013, *102* (1), 012111.

21. Lee, Y. H.; Zhang, X. Q.; Zhang, W.; Chang, M. T.; Lin, C. T.; Chang, K. D.; Yu, Y. C.; Wang, J. T. W.; Chang, C. S.; Li, L. J., Synthesis of Large-Area MoS2 Atomic Layers with Chemical Vapor Deposition. *Advanced Materials* 2012, *24* (17), 2320-2325.

22. Lin, Y.-C.; Zhang, W.; Huang, J.-K.; Liu, K.-K.; Lee, Y.-H.; Liang, C.-T.; Chu, C.-W.; Li, L.-J., Wafer-scale MoS 2 thin layers prepared by MoO 3 sulfurization. *Nanoscale* 2012, *4* (20), 6637-6641.

23. Liu, K.-K.; Zhang, W.; Lee, Y.-H.; Lin, Y.-C.; Chang, M.-T.; Su, C.-Y.; Chang, C.-S.; Li, H.; Shi, Y.; Zhang, H., Growth of large-area and highly crystalline MoS2 thin layers on insulating substrates. *Nano letters* 2012, *12* (3), 1538-1544.

24. Wang, X.; Feng, H.; Wu, Y.; Jiao, L., Controlled synthesis of highly crystalline MoS2 flakes by chemical vapor deposition. *Journal of the American Chemical Society* 2013, *135* (14), 5304-5307.

25. Kretschmann, E.; Raether, H., Radiative decay of non radiative surface plasmons excited by light. *Zeitschrift für Naturforschung A* 1968, *23* (12), 2135-2136.

26. Davis, L. C., Theory of surface-plasmon excitation in metal-insulator-metal tunnel junctions. *Physical Review B* 1977, *16* (6), 2482-2490.

27. Homola, J.; Piliarik, M., Surface plasmon resonance (SPR) sensors. In *Surface plasmon resonance based sensors*, Springer: 2006; pp 45-67.

28. Homola, J.; Koudela, I.; Yee, S. S., Surface plasmon resonance sensors based on diffraction gratings and prism couplers: sensitivity comparison. *Sensors and Actuators B: Chemical* 1999, *54* (1-2), 16-24.

29. Homola, J., Present and future of surface plasmon resonance biosensors. *Analytical and bioanalytical chemistry* 2003, *377* (3), 528-539.

30. Campion, A.; Kambhampati, P., Surface-enhanced Raman scattering. *Chemical society reviews* 1998, *27* (4), 241-250.

31. Zayats, A. V.; Smolyaninov, I. I.; Maradudin, A. A., Nano-optics of surface plasmon polaritons. *Physics reports* 2005, *408* (3-4), 131-314.

32. Maier, S. A., *Plasmonics: fundamentals and applications*. Springer Science & Business Media: 2007.

33. Yan, Z. Plasmonics powered hybrid platform for label free bio-sensing. UCLA, 2017.

34. Le Ru, E.; Etchegoin, P., *Principles of Surface-Enhanced Raman Spectroscopy: and related plasmonic effects*. Elsevier: 2008.

35. Xin, A., *Nanostructured and photoelectrochemical systems for solar photon conversion*. World Scientific: 2008; Vol. 3.

36. Memming, R., *Semiconductor electrochemistry*. John Wiley & Sons: 2015.

37. Vayssieres, L., *On solar hydrogen and nanotechnology*. John Wiley & Sons: 2010.

38. Bak, T.; Nowotny, J.; Rekas, M.; Sorrell, C., Photo-electrochemical hydrogen generation from water using solar energy. Materials-related aspects. *International journal of hydrogen energy* 2002, *27* (10), 991-1022.

39. Kudo, A.; Miseki, Y., Heterogeneous photocatalyst materials for water splitting. *Chemical Society Reviews* 2009, *38* (1), 253-278.

40. Maeda, K.; Domen, K., Photocatalytic water splitting: recent progress and future challenges. *The Journal of Physical Chemistry Letters* 2010, *1* (18), 2655-2661.

41. Chen, Z.; Dinh, H. N.; Miller, E., *Photoelectrochemical water splitting*. Springer: 2013.

42. Ye, P.; Xin, W.; Zheng, L.; Xie, Y.-H., Uniform growth of high-concentration MoS2 nanoflakes on plasma treated carbon nanotube sheet. *Materials Letters* 2019, *256*, 126665.

# Chapter 2 Growth of $MoS_2$ on Carbon Nanotube substrate via Chemical Vapor Deposition methods


## Abstract

In this chapter, we demonstrate a novel two-step approach that is capable of growing uniform high-concentration $MoS_2$ nanoflakes on the carbon nanotube (CNT) sheet substrate. The CNT sheet is simply activated by the oxygen plasma to separate large CNT bundles and to create more active surface sites. A typical chemical vapor deposition (CVD) process is employed, enabling the direct growth of $MoS_2$ nanoflakes on the activated CNT substrate. Morphologies and structures of $MoS_2$/CNT nanohybrid are characterized by SEM/EDS, high-resolution TEM (HRTEM) and Raman spectroscopy. Our results suggest that the plasma treatment of CNT sheet is critical to obtain well-dispersed large quantity of $MoS_2$ nanoflakes on CNT assemblies.


## 2.1 Introduction

Molybdenum disulfide ($MoS_2$), one of the representative transition metal dichalcogenides (TMDs), has attracted increasing research interest in the field of two-dimensional (2-D) nanomaterials[1]. The growth, structures, and emerging applications of

$MoS_2$ have been extensively investigated. In particularly, $MoS_2$ and its composites have been widely employed as anode materials in lithium ion batteries (LIBs)[2,3]. Incorporation of $MoS_2$ with highly conductive carbonaceous materials, such as CNTs and graphene[4,5], can greatly improve the low-conductivity issue caused by $MoS_2$ in LIBs[6,7,8]. Consequently, researchers have devoted great efforts to developing nanocomposites made of $MoS_2$ with these carbon materials, particularly with CNTs[8].

However, it is still challenging to grow high-concentration $MoS_2$ on pristine CNT platforms due to the chemical inertness of CNT walls. CNTs have to be functionalized to get sufficient active spots that can immobilize $MoS_2$[9,10]. Traditional functionalization of CNTs usually contains multiple steps, which is complicated, time-consuming, and costly [11]. Moreover, current research mainly focuses on using loose CNT powder as the support for $MoS_2$ [8,9,10]. To the best of our knowledge, reports on directly growing $MoS_2$ nanostructures on CNT assemblies, i.e. CNT yarns and sheets are very limited. CNT assemblies are the macro-form of individual CNTs, which transfer their excellent mechanical and physical properties from nanoscale to macroscopic scale[12]. Therefore, CNT macroscopic assemblies are the ideal platform to support foreign materials to make novel nanocomposites[13].

In this study, we report a novel approach to directly grow high-concentration $MoS_2$ nanoflakes on the CNT sheet with high uniformity. By using oxygen plasma, we not only increase effective surface areas of the CNT sheet via de-bundling process but also create more active sites to anchor $MoS_2$. The activated CNT sheet is then employed as the substrate and $MoS_2$ nanoflakes can uniformly grow on it through a CVD process.

Compared with untreated CNT sheet, both uniformity and concentration of $MoS_2$ are significantly improved on the substrate of plasma treated CNT sheet.

## 2.2 Experimental

### 2.2.1 Chemicals and Materials

CNT sheet was received from Nanocomp Technologies Inc. (Merrimack, NH), which was fabricated by a continuous CVD process. Sulfur (S, 99.998%) and molybdenum oxide ($MoO_3$, 99.97%) were purchased from Sigma-Aldrich. The materials were used as received without any treatment or purification.

### 2.2.2 Plasma treatment of CNT sheet.

CNT sheet was first cut into the dimension of 10 cm × 2.54 cm. The plasma treatment was performed by Atomflo™ plasma system (Surfx® Technologies LLC) with the power of 150 W, helium gas feeding rate at 30 L/min and oxygen at 0.5 L/min. Plasma scanning rate was 20 mm/s and the total exposure time was 90 s for one side. Double-side treatment was carried out. The plasma treatment is schematically shown as Figure 2.1, step 1.

### 2.2.3 $MoS_2$ growth on the CNT sheet substrate.

We use traditional CVD method to grow $MoS_2$ on the CNT sheet substrate. The equipment set-up is schematically shown in Figure 2.1 (step 2). In short, 10 mg $MoO_3$ powder and 500 mg S powder were used as Mo and S precursors, respectively. The CNT sheet was put up-side down facing towards the $MoO_3$ powder localized at the furnace center. The substrate temperature is set to be 850 $^oC$, while S powder was put at the temperature window, where the T was set as 200 $^oC$. The total growth time was 15min. During the growth, Ar was employed as the carrier gas with a flow rate of 100 sccm.

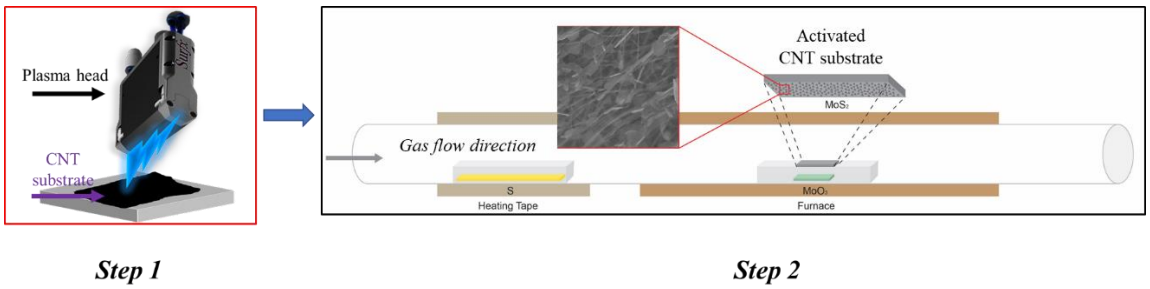


Figure 2. 1 Schematic illustration of two-step approach for $MoS_2$ growth on the CNT sheet.

2.2.4 Characterizations

Scanning electron microscopy (SEM) images coupled with related energy dispersive X-ray (EDS) analysis of the samples were obtained from FEI Nova NanoSEM 230. Transmission electron microscopy (TEM) and high-resolution transmission electron microscopy (HRTEM) images were captured with FEI Titan S/TEM system at 200 keV. Raman spectroscopy analysis was obtained with a Renishaw In-Via Raman system with the laser length of 633 nm and laser power of 1mW at objective lens magnification of 50x and a grating spacing of 1200 *l*/mm.

2.3 Result and Discussion

Figure 2.2 (a) is the photograph of a typical spool of raw CNT sheet obtained from the supplier. From the microstructure of raw CNT sheet shown in Figure 2.2 (b) and (c), one can see the condensed network composed of CNT bundle. In these bundles, individual CNTs are bonded together by van de Waals interaction[12]. After plasma treatment (Figure 2.2 (d) and (e)), nanotubes are uniformly separated apart from original bundles, which is a so-called "de-bundling" process. The de-bundling would significantly enhance the effective surface area of CNT sheet, as schematically shown in Figure 2.2 (f). Another

benefit from plasma treatment is the creation of more defective but active sites, which will be discussed in details shortly.

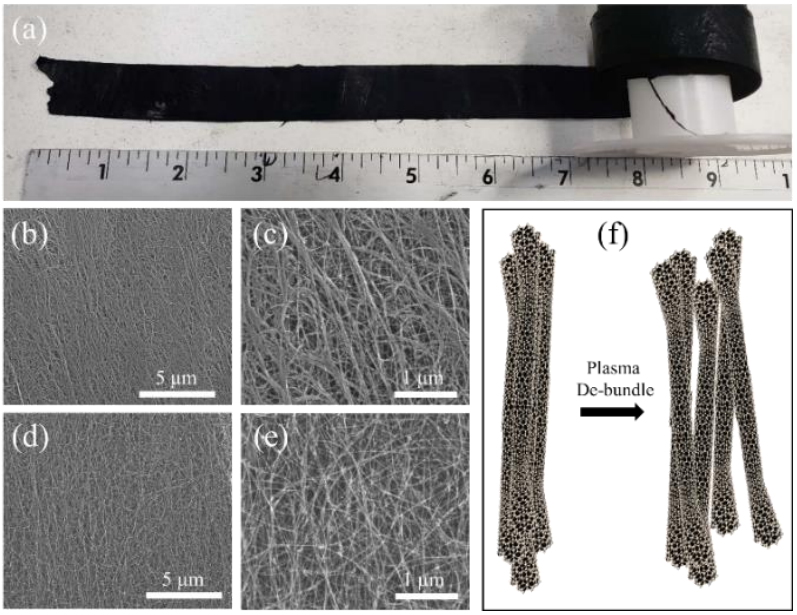


Figure 2. 2 (a) Photography of CNT sheet spool. (b) Low- and (c) High- magnification of SEM images of raw CNT sheet. (d) Low- and (e) High- magnification of SEM images of plasma activated CNT sheet. (f) De-bundling process induced by plasma treatment.

We now investigate the growth of $MoS_2$ on the CNT sheet substrate. Firstly, $MoS_2$ can grow on the raw CNT sheet. Their distribution on the CNT support, however, is quite non-uniform as shown in Figure 2.3 (a). In addition, they demonstrate very distinguishable shapes and sizes. These $MoS_2$ nanostructures aggregate on the CNT bundles (Figure 2.3 (b)), creating large domains that are free of $MoS_2$ (Figure 2.3 (d)). Such a poor dispersion of $MoS_2$ can be identified from the EDS result in Figure 2.3 (i), where only a few particles have signals of S and Mo. Interestingly, we find a large ratio of $MoS_2$ nanoflakes vertically

aligned to the CNT surface (Figure 2.3 (c)). The measured thickness of a selected $MoS_2$ nanoflake is ~ 55 nm.

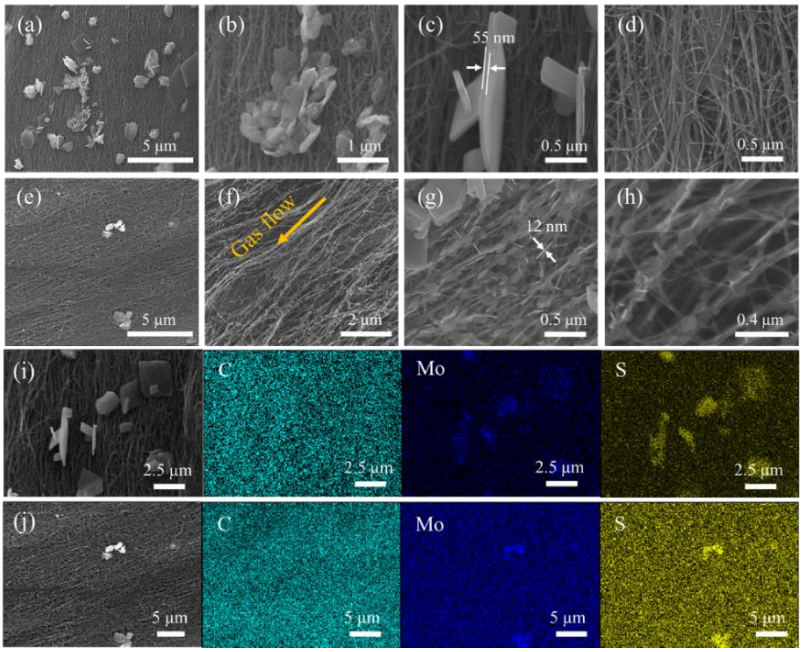


Figure 2. 3 Microstructures and elemental analysis of $MoS_2$ on CNT sheet. (a)-(d) SEM images of $MoS_2$ grown on raw CNT sheet. (e)-(h) SEM images of $MoS_2$ grown on plasma treated CNT sheet. (i) Elemental analysis of raw CTN sheet/ $MoS_2$. (j) Elemental analysis of activated CTN sheet/ $MoS_2$.

In contrast, a large quantity of $MoS_2$ nanoflakes are uniformly deposited on the substrate of plasma treated CNT sheet, as illustrated in Figure 2.3 (e). It is of interest to note that $MoS_2$ nanoflakes are successfully grafted on almost every individual CNTs and CNT bundles (Figure 2.3 (f)-(h)). The measured thicknesses of nanoflakes are in the range of 10-14 nm. It is reasonable to observe the thickness differences between $MoS_2$ sheets on

different CNT substrates, as the incoming $MoS_2$ molecules prefer to land on the as-nucleated $MoS_2$ islands instead of on inert CNT walls. With the treatment, anchoring sites on the CNT sheet for $MoS_2$ molecules are enhanced significantly. As a result, MoS2 sheets are distributed more uniformly with thinner features. EDS result in Figure 2.3 (j) not only identifies nanoflakes are $MoS_2$ but also confirms the uniform dispersion of these nanoflakes, as overall intensities of S and Mo signals are homogenously distributed on the entire substrate. $MoS_2$ signal from the EDS spectrum of plasma treated sample is much more striking than that of raw CNT sheet/ $MoS_2$ (Figure 2.4), suggesting the significantly improved concentration of $MoS_2$.

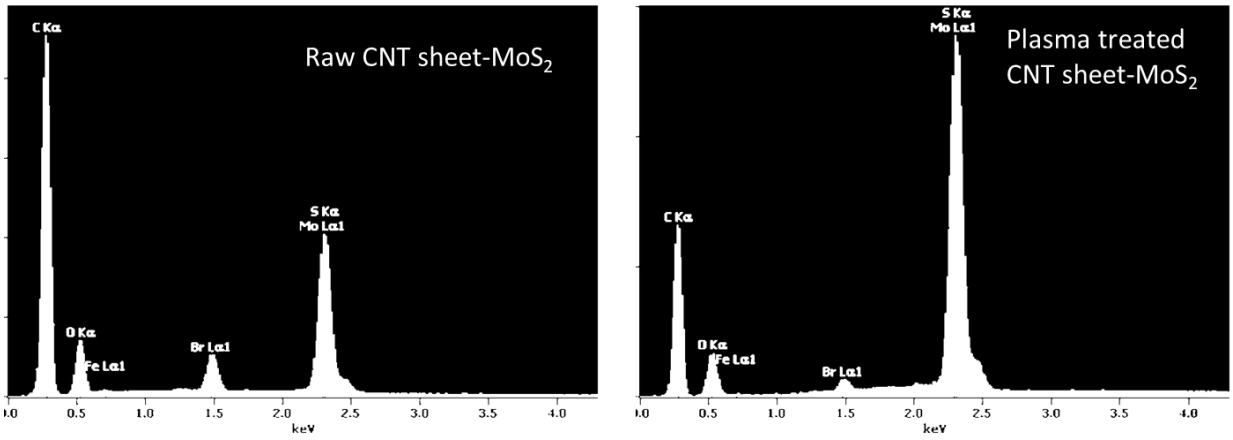


Figure 2. 4 EDX spectra of raw CNT sheet-$MoS_2$ and plasma treated CNT sheet-$MoS_2$.

Besides of de-bundling effect, another important change of the CNT sheet before and after plasma treatment is captured by Raman scattering. $I_D$ / $I_G$ (intensity of the D peak/ intensity of the G peak) characterizes the ratio of disorders of $sp^2$ carbon network of crystalline carbon materials[14]. As shown in Figure 2.5 (a), $I_D$ / $I_G$ of CNT sheet increases from 0.06 to 0.58 after the plasma activation. The enhancement is attributed to the

introduction of oxidized species such as carboxyl and hydroxyl groups[15]. These functional groups make CNT surfaces more suitable to nucleate and immobilize external nano-species. In our study, de-bundling and oxidization from plasma treatment are the two key points that enable us to obtain high-concentration $MoS_2$ nanoflakes uniformly grown on the CNT sheet.

Figure 2.5 (b) presents the overall comparison of Raman scattering between raw CNT sheet deposited with $MoS_2$ ($R_{CNT}$- $MoS_2$) and plasma treated CNT sheet deposited with $MoS_2$ ($P_{CNT}$- $MoS_2$). Intensity of $MoS_2$ in the sample $R_{CNT}$- $MoS_2$ are barely identified (Figure 2.5 (c)), indicating very low concentration of $MoS_2$ grown successfully. In contrast, peaks at 373 $cm^{-1}$ and 402 $cm^{-1}$ of $P_{CNT}$- $MoS_2$ are ascribed to $E^1_{2g}$ and $A_{1g}$ modes of $MoS_2$, respectively, which, once again, identify the existence of $MoS_2$. Moreover, the signal intensity scattered from $MoS_2$ is comparable to the G peak of the CNT, elucidating the existence of extremely high concentration of $MoS_2$. Interestingly, the ratios of $I_D$ / $I_G$ in the two samples are both enhanced after the grating of $MoS_2$ (Figure 2.5 (e)), which implies the deposition of $MoS_2$ on CNT support may degrade the crystallinity or integrity of the nanotubes.

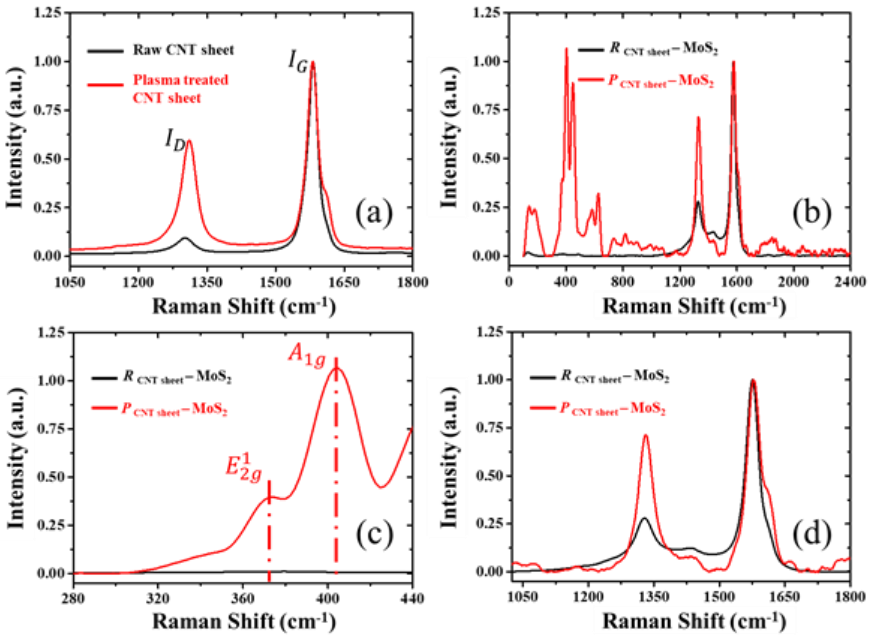


Figure 2. 5 Raman spectroscopy characterizations of (a) D and G peaks of raw sheet and plasma activated sheet. (b) Raw sheet/$MoS_2$ ($R_{CNT}$- $MoS_2$) and plasma activated sheet/$MoS_2$ ($P_{CNT}$- $MoS_2$) in the frequency 100- 2400 cm$^{-1}$ (c) 280- 440 cm$^{-1}$ (d) 1050- 1800 cm$^{-1}$.

Figure 2.6 (a) shows the representative TEM image of $MoS_2$ nanoflakes deposited on the plasma treated CNT support, from which we observe two hexagonal $MoS_2$ nanoflakes with lateral sizes of 135 nm and 157 nm, respectively. They are highly transparent under 200 keV electron beam because of the ultrathin nature. The edge as well as the corner of ultrathin $MoS_2$ nanoflake can be observed from Figure 2.6 (b). A high-magnification image in Figure 2.6 (c) presents the atomic structure of $MoS_2$ and the insert is its corresponding fast Fourier transformation (FFT) pattern. The typical six-fold symmetry is confirmed from the FFT, suggesting a single-crystalline nanoflake[16]. More

importantly, the yellow dotted line highlights CNT-$MoS_2$ interface at the atomic scale. $MoS_2$ is not perfectly straight but has a few layers impinged into CNT walls, which may cause the degradation of CNT crystallinity. This likely drives the increase of $I_D$ / $I_G$ as discussed in Figure 2.5 (d). Further analysis in Figure 2.6 (d) shows the lattice distance of $MoS_2$ is 2.7 Å, which can be assigned to $MoS_2${100} planes and corresponds to the six-fold spots of the FFT pattern[17].

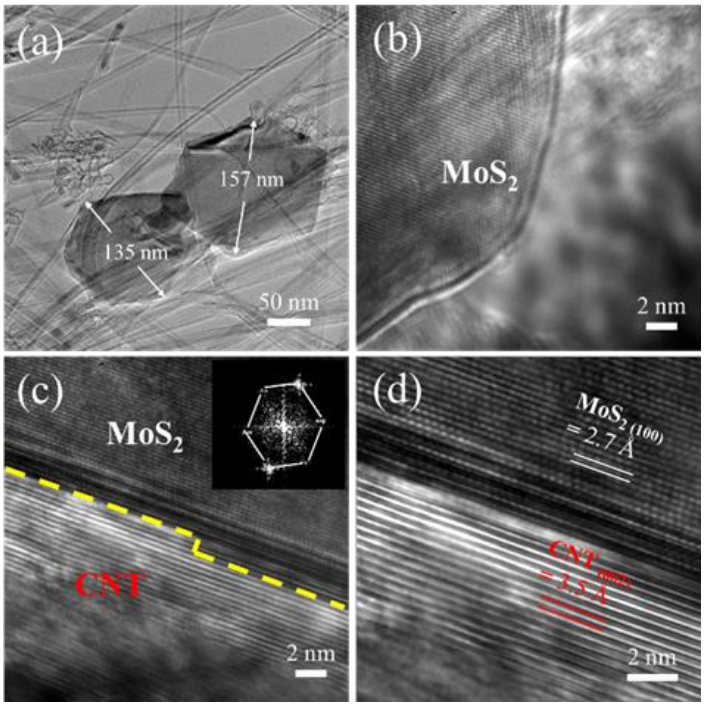


Figure 2. 6 TEM study of CNT-MoS2 interfaces. (a) Representative TEM image of $P_{CNT}$-$MoS_2$. (b) $MoS_2$ edge and corner. (c) High-resolution TEM image of CNT-$MoS_2$ interface. (d) Lattice distance of $MoS_2$ captured by HRTEM.

## 2.4 Conclusion

In summary, we report a facile strategy to uniformly grow $MoS_2$ nanoflakes on plasma activated CNT sheet. We demonstrate that plasma induced de-bundling as well as defective sites on the CNT sheet are two critical keys to obtain high-concentration and uniform $MoS_2$ nanoflakes on the assembly of CNTs. This work may shed light on the controllable synthesis of $MoS_2$/carbon nanocomposites as well as their related applications in battery fields.

## 2.5 References


1. Xia, F.; Wang, H.; Xiao, D.; Dubey, M.; Ramasubramaniam, A., Two-dimensional material nanophotonics. *Nature Photonics* 2014, *8* (12), 899.

2. Xiao, J.; Choi, D.; Cosimbescu, L.; Koech, P.; Liu, J.; Lemmon, J. P., Exfoliated MoS2 nanocomposite as an anode material for lithium ion batteries. *Chemistry of Materials* 2010, *22* (16), 4522-4524.

3. Mishra, R. K.; Krishnaih, M.; Kim, S. Y.; Kushwaha, A. K.; Jin, S. H., Binder-free, scalable hierarchical MoS2 as electrode materials in symmetric supercapacitors for energy harvesting applications. *Materials Letters* 2019, *236*, 167-170.

4. Xin, W.; De Rosa, I. M.; Cao, Y.; Yin, X.; Yu, H.; Ye, P.; Carlson, L.; Yang, J. M., Ultrasonication-assisted synthesis of high aspect ratio gold nanowires on a graphene template and investigation of their growth mechanism. *Chem Commun (Camb)* 2018, *54* (33), 4124-4127.

5. Xin, W.; De Rosa, I. M.; Ye, P.; Severino, J.; Li, C.; Yin, X.; Goorsky, M. S.; Carlson, L.; Yang, J. M., Graphene template-induced growth of single-crystalline gold nanobelts with high structural tunability. *Nanoscale* 2018, *10* (6), 2764-2773.

6. Chen, X.; Li, L.; Wang, S.; Feng, C.; Guo, Z., Synthesis and electrochemical performances of MoS2/C fibers as anode material for lithium-ion battery. *Materials Letters* 2016, *164*, 595-598.

7. Chang, K.; Chen, W., L-cysteine-assisted synthesis of layered MoS2/graphene composites with excellent electrochemical performances for lithium ion batteries. *ACS nano* 2011, *5* (6), 4720-4728.

8. Patel, M. D.; Cha, E.; Kang, C.; Gwalani, B.; Choi, W., High performance rechargeable Li-S batteries using binder-free large sulfur-loaded three-dimensional carbon nanotubes. *Carbon* 2017, *118*, 120-126.

9. Gong, L.; Wang, L.; Lu, J.; Han, C.; Chen, W.; Sow, C. H., Photocurrent response in multiwalled carbon nanotube core–molybdenum disulfide shell heterostructures. *The Journal of Physical Chemistry C* 2015, *119* (43), 24588-24596.

10. Li, J.; Hou, Y.; Gao, X.; Guan, D.; Xie, Y.; Chen, J.; Yuan, C., A three-dimensionally interconnected carbon nanotube/layered MoS2 nanohybrid network for lithium ion battery anode with superior rate capacity and long-cycle-life. *Nano Energy* 2015, *16*, 10-18.

11. Datsyuk, V.; Kalyva, M.; Papagelis, K.; Parthenios, J.; Tasis, D.; Siokou, A.; Kallitsis, I.; Galiotis, C., Chemical oxidation of multiwalled carbon nanotubes. *Carbon* 2008, *46* (6), 833-840.

12. Lekawa-Raus, A.; Patmore, J.; Kurzepa, L.; Bulmer, J.; Koziol, K., Electrical properties of carbon nanotube based fibers and their future use in electrical wiring. *Advanced Functional Materials* 2014, *24* (24), 3661-3682.

13. Xin, W.; Yang, J. M.; Li, C.; Goorsky, M. S.; Carlson, L.; De Rosa, I. M., Novel Strategy for One-Pot Synthesis of Gold Nanoplates on Carbon Nanotube Sheet As an Effective Flexible SERS Substrate. *ACS Appl Mater Interfaces* 2017, *9* (7), 6246-6254.

14. Xin, W.; Severino, J.; De Rosa, I. M.; Yu, D.; McKay, J.; Ye, P.; Yin, X.; Yang, J. M.; Carlson, L.; Kodambaka, S., One-Step Synthesis of Tunable-Size Gold Nanoplates on Graphene Multilayers. *Nano Lett* 2018, *18* (3), 1875-1881.

15. Yu, H.; Cheng, D.; Williams, T. S.; Severino, J.; De Rosa, I. M.; Carlson, L.; Hicks, R. F., Rapid oxidative activation of carbon nanotube yarn and sheet by a radio frequency, atmospheric pressure, helium and oxygen plasma. *Carbon* 2013, *57*, 11-21.

16. Xin, W.; De Rosa, I. M.; Ye, P.; Zheng, L.; Cao, Y.; Cao, C.; Carlson, L.; Yang, J.-M., Simplified fabrication strategy of graphene liquid cells for the in situ transmission electron microscopy study of Au nanoparticles. *The Journal of Physical Chemistry C* 2019, *123* (7), 4523-4530.

17. Huang, X.; Zeng, Z.; Bao, S.; Wang, M.; Qi, X.; Fan, Z.; Zhang, H., Solution-phase epitaxial growth of noble metal nanostructures on dispersible single-layer molybdenum disulfide nanosheets. *Nature communications* 2013, *4* (1), 1-8.

# Chapter 3 One-pot Self-templated Growth of Gold Nano-frames For Enhanced SERS Performance


## Abstract

As one of the representative metallic hollow nanostructures, Au nanoframes have shown fascinating properties such as strong localized surface plasmon resonance (LSPR) associated with the emerging application as surface-enhanced Raman scattering (SERS) sensors. In this study, it is demonstrated, for the first time, a facile one-pot synthetic approach for hollow Au nanoframes by directly etching Au nanoplates, i.e. so-called self-templates. A novel growth mechanism has been revealed that involves a synergistic function of Ag and Br ions. The presence of $Ag^+$ lead to observed self-limiting of Au film thickness whereas Au {111} facets are preferentially attacked by the presence of $Br^-$ in the reaction ambient. Moreover, graphene is introduced to prevent/minimize aggregation during the formation of Au nanoframes. Combined simulation and experimental studies show that the hybrid platform made of graphene/Au nanoframes is capable of detecting analytes at concentration levels down to $10^{-9}$ M by using the surface-enhanced Raman spectroscopy (SERS) technique.

## 3.1 Introduction

Hollow nanostructures have attracted increasing research interest recently owing to their unique characteristics[1,2], such as large surface area, high fraction of active surface sites, low density, well-controlled dimensions, and multi-functional properties as nano-reactors[3,4], catalysis[5,6], and sensors[7]. A variety of strategies have been developed to fabricate hollow nanostructures, including top-down lithography[8], nanowires self-coiling[9], self-assembly processing[10], galvanic replacement[11-13], and chemical etching[14-20]. Particularly, to create metallic hollow structures on the nanoscale, chemical etching is the most commonly employed approach[21]. It has been witnessed that ultrathin Au nanoframes[14,15], shape-controllable nanoframes of Au[16], Pt[17], and Pd[18], complex trimetallic nanoframes such as Au@Pt-Ni[19] and AgAu@Pt[20] core-shell alloys, hierarchical 4H/fcc Ru nanotubes[22], and so forth, are successfully synthesized via the template carving Such hollow metal nanostructures present tunable optical properties[16], enhanced plasmonic and catalystic activies[23], robust surface-enhanced Raman scattering (SERS) performance[24], and increased electrocatalytic effects[25].

In the science of carving metal nanocrystals, chemical etching by corrosive chemicals such as hydrogen peroxide[15] and oxidative etching by the conjunction of oxygen and halogen ($Cl^-$, $Br^-$, and $I^-$) ions[18], [26-28] are realized at the expense of inside solid blocks, namely, sacrifice templates within the enclosed frames. These synthetic strategies are widely adopted to fabricate Au nanoframes, which is one of the representative hollow metal nanostructures that are studied intensively. For instance, Xue and co-authors obtained ultrathin Au nanoframes with tailorable widths in the range of 1.8 – 6.0 nm using Ag nanoplates as the sacrifice template[14]. Nie et al. reported the synthesis of circular and

triangular Au nanorings by excavating templates of Ag nanodisks and Ag nanoprisms, respectively[16]. In these approaches, however, materials of the sacrificial templates are different from the nanoframes, which cost extra steps for the preparation, causing difficulty in the controlling of the chemical synthesis due to the homogeneous nucleation of the coating material[2]. Moreover, these methods usually involve multiple cycles of metal deposition and etching[29], which may significantly reduce the reproducibility and make it difficult to scale-up.

Herein, we demonstrate a one-pot strategy for the growth of Au nanoframes, Relying on the etching of Au nanoplates, i.e. self-templates. Well-defined Au nanoplates with tunable thickness are first synthesized. In the same solution, Au nanoplates can be gradually etched to Au nanoframes over time. With a systematically study, we reveal both $Ag^+$ and $Br^-$ ions are of critical importance to the synthesis. Moreover, we employ graphene template to reduce the aggregation of Au nanoframes. As a consequence, we show the hybrid platform made of graphene/Au nanoframes provides excellent SERS performance.

## 3.2 Experimental

### 3.2.1 Chemicals and Materials

Graphene template (AO-2) was purchased from Graphene Supermarket (Calverton, New York). Gold chloride hydrate ($HAuCl_4 \cdot xH_2O$, 99.999%), silver nitrate ($AgNO_3$, ≥ 99.0 %), potassium bromide (KBr, ≥ 99.0 %), and potassium iodide (KI, ≥ 99.0 %) were purchased from Sigma-Aldrich, USA. L-ascorbic acid (> 99.0%) and Rhodamine 6G (99 %) were obtained from Fisher Scientific, USA.

3.2.2 Experimental Procedures

One-step synthesis of Au nanoframes: In a standard procedure, we first prepared 18 mL deionized (DI) water in a glass vial. Then, 85.5 μM $HAuCl_4$ (60 μL, 28.5 mM), 85.5 μM KBr (50 μL, 30 mM), and 125 μM $AgNO_3$ (250 μL, 10 mM) were added to the vial. After the mixture was homogeneous mixed with gently shaking, 500 μL ascorbic acid (0.4 mM) was then added to the solution. The glass vial was capped with a PTFE lined cap and placed in an oven at 80 $^oC$ for 1 hours for the hydrothermal reduction. Subsequently, the glass vial was taken out from the oven and aged at room temperature for different time, i.e. 4 hrs, 24 hrs, 48 hrs and 96 hrs, to enable the etching.

In order to verify the roles of $Ag^+$ ions, more samples were prepared with 5 μM, 20 μM, 50 μM, 400 μM, and 800 μM $AgNO_3$, while keeping the concentrations of all other chemicals as well as the reaction condition the same. At the same time, to explore $Br^-$ ions function, a series of samples were prepared by only changing KBr concentrations as 0 μL, 10 μL, 200 μL, and 500 μL. Moreover, NaI providing an equivalent amount of $I^-$ ions was used to replace KBr in the synthesis, in order to comprehensively demonstrate the role of the $Br^-$ ions.

One-pot synthesis of Au nanoframes on graphene template: To improve the aggregation, we introduced graphene multilayers as the template for Au nanoframes. The synthesis was slightly modified from the previous section. First, 1 mg graphene powder is added into the glass vial containing 18 mL DI water and the mixture was ultrasonicated for 1 minute to obtain well-dispersed suspension. Thereafter, the same amount of chemicals, i.e. $HAuCl_4$ (60 μL, 28.5 mM), KBr (50 μL, 30 mM), $AgNO_3$ (250 μL,10 mM), and ascorbic acid (500 μL, 0.4 mM) were added to the vial. The mixture was capped closely

and then maintained in the oven at 80 $^{o}$C for 1 hr. After that, the sample was taken out from the oven and placed at room temperature for 48 hr. Then the synthesized hybrid material was washed and collected by centrifugation for further characterization and other usage.

3.2.3 Characterizations

Surface-enhanced Raman scattering (SERS) performance: The synthesized graphene/Au nanoframes suspension was deposited on a silicon (Si) substrate with [100] orientation using a pipette. The Si supported hybrid was dried in the vacuum oven at 100 $^{o}$C for 2 hours. The deposition process was repeated by 3 times to assure the substrate was totally covered with graphene/Au nanoframes. To test the SERS performance, a highly fluorescent dye material, Rhodamine 6G (R6G) aqueous solution (20 μL) was deposited on five prepared substrates, at the concentrations of $10^{-5}$ M, $10^{-6}$ M, $10^{-7}$ M, $10^{-8}$ M and $10^{-9}$ M, respectively. The substrates were transferred to Raman equipment before the R6G solution was fully dried. Spots deposited with Au nanoframes can be observed from the optical microscope. When performing Raman scattering, we particularly check these spots and record the Raman signals of the analyte. Raman scattering spectra were obtained with a Renishaw In-Via Raman system with the laser length of 785 nm, expose time of 10 s, laser power of 1mW, objective lens magnification of 50 ×, and a grating spacing of 1200 *l*/mm.

Simulation of Plasmonic Properties of Au nanoframes: The near field electromagnetic field distribution was simulated via finite difference time domain simulation (Lumerical FDTD simulations). The perfect match layer (PML) was set as the absorptive boundary. The mesh size was set at 0.1 nm × 0.1 nm × 0.1 nm within the simulation area (plate/frame area). The edge lengths of Au nanoplates were appointed as 20 nm and 34.64 nm for

hexagonal and triangular shapes, respectively. Both of them had the thickness of 10 nm. The nanoframes had the same lateral sizes with the frame width of 10 nm. The dielectric function of Au was obtained from Johnson and Christy. Graphene was used as the substrate and its dielectric constant was taken from Falkovsky. The simulation result is the E/E0 distribution along the top surface of the plate/frame structure.

Characterizations: Top and tilt view scanning electron microscopy (SEM) images of samples with different *t* were obtained with FEI Nova NanoSEM 230. The system was coupled with an energy dispersive X-ray (SEM/EDX) detector (ThermoFisher Scientific), which can monitor spatial elemental maps of Au nanoplates, Au nanoframes and graphene supported Au nanoframes. Transmission electron microscopy (TEM) and high-resolution transmission electron microscopy (HRTEM) images were captured with FEI Titan S/TEM system at 300 keV. The X-ray diffraction (XRD) measurements were performed on a Bruker D1 diffractometer using Cu Kα1 radiation.

## 3.3 Result and Discussion

The details of the one-pot synthetic approach are revealed in the supporting information. We first investigate Au templates prior to the etching. At the time $t$ = 4 h, well-defined two-dimensional Au nanoplates are obtained with a yield > 90%, as shown in Figure 3.1(a). It is of interest to note such a high yield of Au nanoplates is extremely difficult to obtain with seedless growth method unless a proper etchant is involved[30]. These nanoplates typically possess triangular and hexagonal shapes with a lateral size of a few microns. Figure 3.1(b) shows a 3-D simulation of two representative Au nanoplates, indicative of relatively smooth and flat surfaces. In addition, 2θ-ω XRD scan of the sample

in Figure 3.1(a) shows the synthesized nanoplates have face-centered cubic (FCC) structure, owing to the peaks observed at 2θ = 38.3°, 44.5°, 82.1°, which belong to Au (111), Au (200), and Au (222), respectively (Figure 3.1(c))[31,32]. It is noteworthy to emphasize the presence of strikingly intensive Au (111) peak. The relative intensity of (111) / (200) is more than 20, indicating the Au nanoplates are predominantly (111) orientated[33]. Inset of Figure 3.1(c) is the elemental mapping from EDX measurement, confirming the nanoplates are pure gold. TEM selected area diffraction pattern of a selected Au nanoplate in Figure 3.1(d) shows diffraction spots of 1/3 (422) and (220) with six-fold symmetry, suggesting an FCC structure, which is consistent with the XRD result. This also indicates the diffracted facet, i.e. the basal plane of the plate is Au (111), which is the predominant crystallographic orientation. The measured lattice distance is 1.44 Å, corresponding to the plane distance of Au (220).[34]

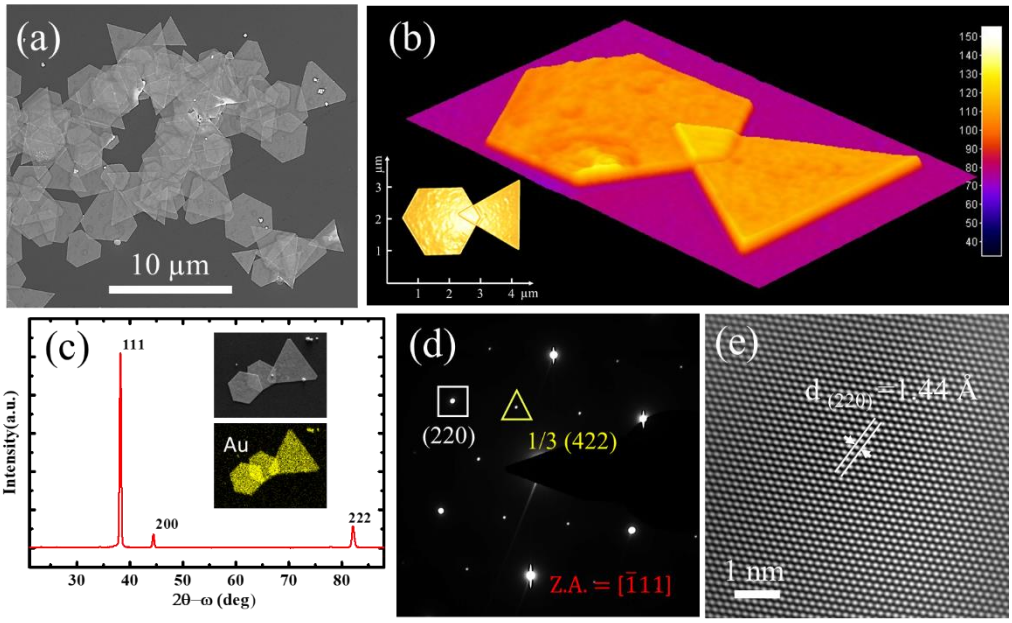


Figure 3. 1 (a) A representative SEM image of Au nanoplates assembly. (b) 3-D simulation profile of two representative Au nanoplates. Simulation is obtained from the SEM image.

(c) X-ray diffraction (XRD) 2θ-ω scan obtained from the Au nanoplates. Inset is the element mapping from EDX. (d) Selected area electron diffraction pattern (SAED) of a nanoplate. (e) The atomic structure on the surface of Au nanoplate obtained from HRTEM.

We now focus on the transformation of Au nanoplates to Au nanoframes *via* the etching process. To begin, we point out that it is the $Br^-$ ion that plays the role of the etchant in our system. It is well established that halogen ions mainly impose two functional roles in the growth of noble metal nanocrystals: the capping agent[35] as well as the etchant[28]. As the capping agent, they would preferentially adsorb on certain facets of the nanocrystals and promote growth in directions other than the passivated facets. In our study, a proper amount of $Br^-$ ions can facilitate the formation of Au nanoplates, for example, where belt-like Au crystallites (Figure S3.1(a)) transform to Au nanoplates (Figure S3.1(b)) when using 15 μM KBr during the synthesis. On the other hand, the etching effect from overdosed Br- ions causes severe damage to the Au nanoplates when more than 750 μM KBr is used (Figures S3.2(c) and (d)).

It is thus very important to employ the appropriate concentration of $Br^-$ ions to obtain desirable Au nanoframes. Accordingly, not only high-yield Au nanoplates (the self-templates) can be synthesized (Figure3. 1(a)), but also well-defined hollow structured Au nanoframes (Figures 3.2(a)-(c)) are produced after etching at room temperature for 48 hrs. It is not surprising to note that the etching effect predominantly depends on the time *t*, as shown in Figure 3.2(d)-(g) with the $t$ = 4, 24, 48, and 96 hrs, respectively. In particular, we observe flat Au nanoplates

transform to concave nanoplates first (Figure 3.2(e) and Figure S3.2, 24 hrs), followed by the formation of center-hollowed Au nanoframes (Figure 3.2(f), 48 hrs). Interestingly, the thinner edge can be carved out, resulting in open frames when *t* extends to more than 96 hrs (Figure 3.2(g)). Selected examples of the etched Au nanoplates are shown in Figure 3.2(h), which suggests the etching is quite uniform at the very beginning but gradually becomes inhomogeneous. This is likely due to the non-uniformity of the thickness of Au nanoplates.

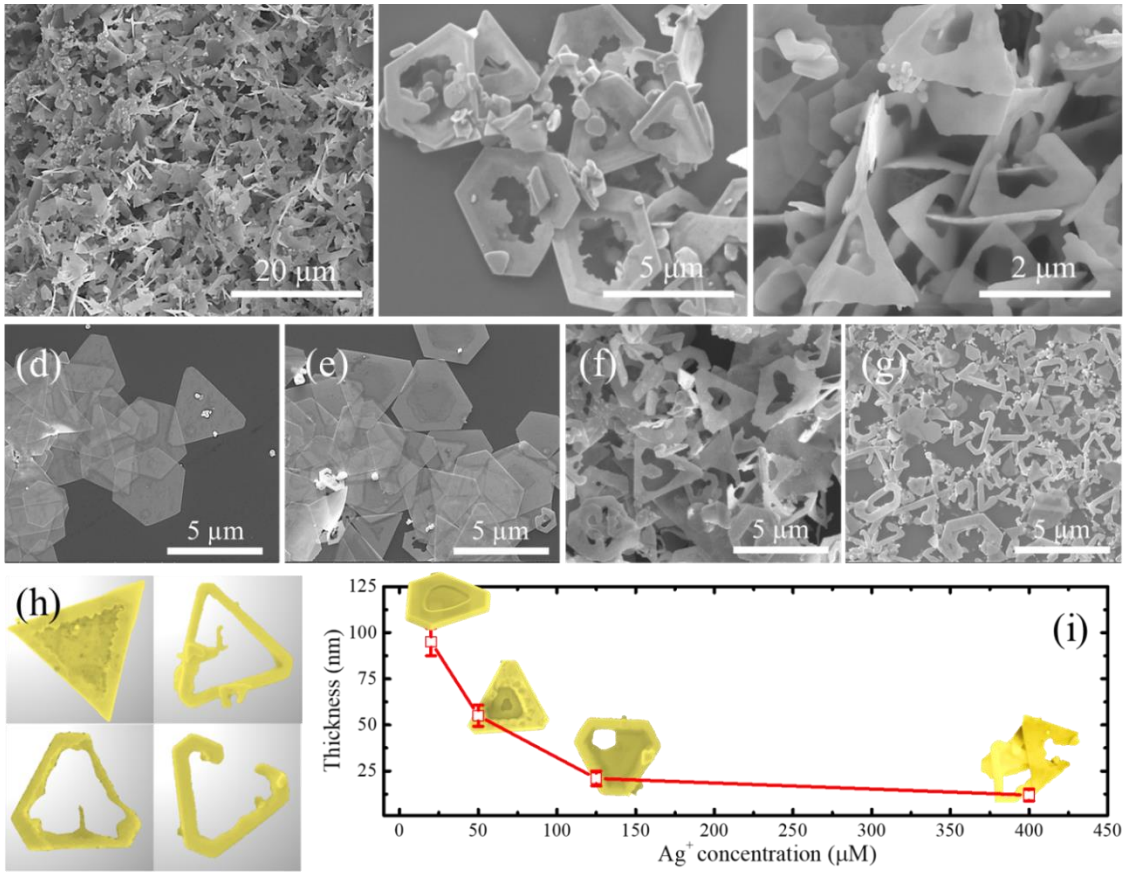


Figure 3. 2 (a)-(c) Representative SEM images of Au nanoframes from low magnification to high magnification. Au nanoplates at the etching time t (d) 4 hrs, (e) 24 hrs, (f) 48 hrs,

and (g) 96 hrs. (h) Four examples of etched Au nanoplates at different stages. (i) Dependence of Au nanoplates' thickness and the etching efficiency on Ag+ concentration.

In our synthesis, the $Ag^+$ ion plays a critical role as well in the formation of Au nanoframes. First, we observe well-defined Au nanoplates can be only synthesized with an appropriate amount of silver ions. Neither less than 20 μM nor more than 800 μM $AgNO_3$, can be used to produce high-quality Au nanoplates (Figure S3.3). Second, the thickness of Au nanoplates is tunable from ~100 nm to ~10 nm, simply by varying the concentration of $AgNO_3$ in the solution from 20 μM to 400 μM (Figure 3.3). In addition, we find the etching efficiency is closely related to the original thickness of Au nanoplates, which increases with the decreasing thickness (Figure 3.2(i)). As a result, Au nanoplates with the thickness > 50 nm can be only partly carved in 48 hrs, leaving a pit hole with irregular shapes on the surface. In contrast, a complete hole or hollow structure from the surface to the bottom is created on nanoplates with the thickness < 50 nm during the same aging period. However, when the thickness is less than 10 nm, the etching becomes more difficult to control and a large number of open nanoframes are obtained.

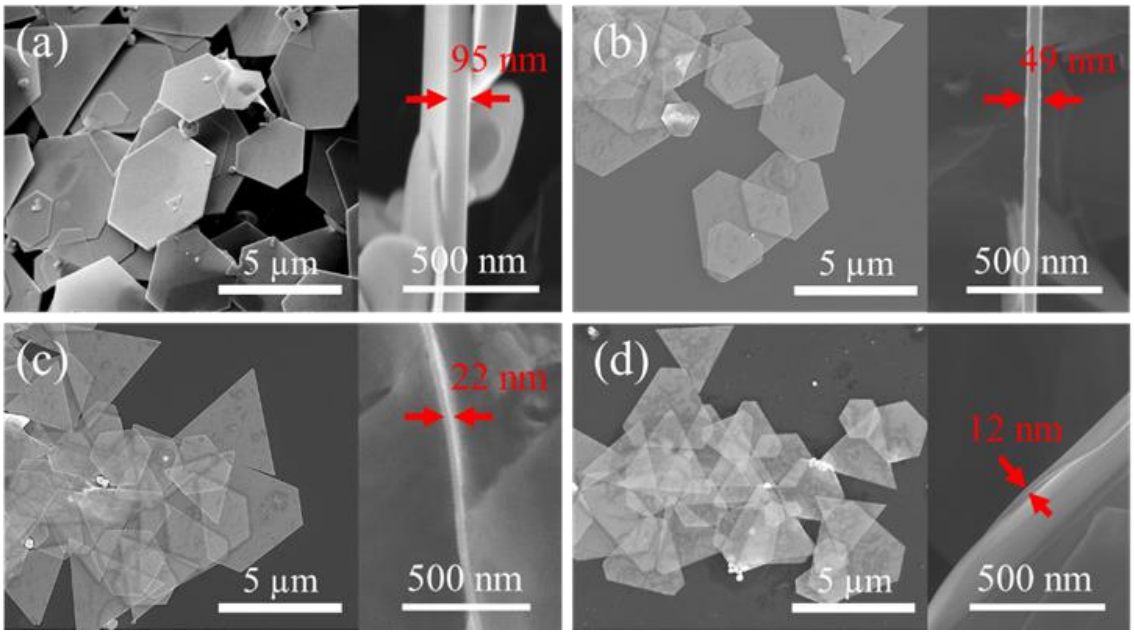


Figure 3. 3 Thickness tunability of Au nanoplates by varying concentrations of $AgNO_3$. (a) 20 μM, (b) 50 μM, (c) 125 μM and (d) 400 μM of $AgNO_3$. The aging time of all samples shown here is 4 hrs.

According to the above results, we propose a growth mechanism of Au nanoframes that involves a synergistic effect of $Ag^+$ and $Br^-$ ions. In particular, $Br^-$ ion serves as the etchant and dictates the etching rate, while $Ag^+$ ion determines the total amount of gold template that is going to be etched up. Figure 3.4 is the schematic illustration of the etching mechanism that highlights individual roles of $Ag^+$ and $Br^-$ ions. In the shape-controlled synthesis of nanoparticles, it is widely known that $Ag^+$ ions, even at a trace amount, can boost the growth of anisotropic gold nanostructures in a high-yield[36-38], including Au nanorods, bipyramids, nanoprisms, ultrathin nanowires, and crystallographic high-index nanoparticles.

Thus far, however, there has been very limited report to reveal $Ag^+$ ions are capable of tailoring the thicknesses of Au nanoplates. The origin of the anisotropy of gold nanostructures directed by $Ag^+$ ions has been an elusive and controversial topic ever since it was discovered[39]. Silver ions ($Ag^+$), complex pair of Ag-Br, and elemental silver ($Ag^0$) that passivate certain facets of gold nanocrystals and promote the growth of anisotropic structures are all considered the plausible mechanisms[40]. Here, it is likely that free $Ag^+$ ions or AgBr could adsorb on Au (111) facets, prevent gold atoms adding to (111) surface, and thus reduce the thickness of the plates accordingly. Nevertheless, the explicit mechanism of $Ag^+$ ion that controls the thickness of Au nanoplates requires an in-depth study, which is out the scope of this research.

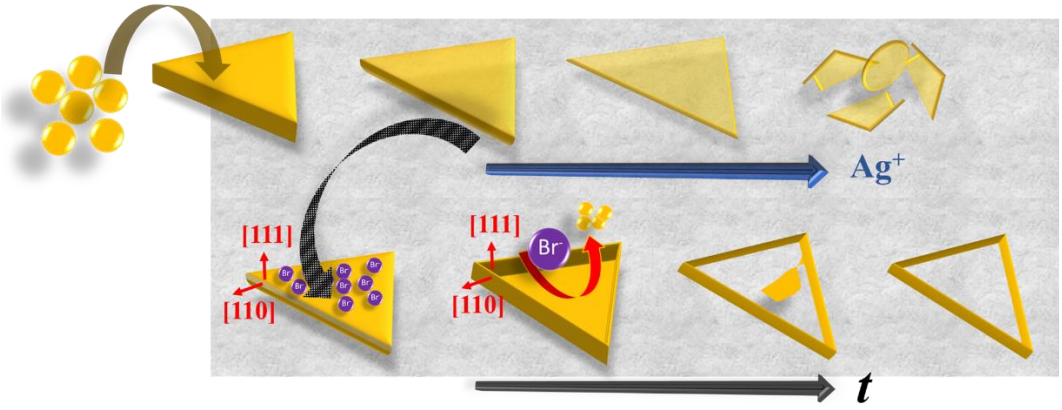


Figure 3. 4 Schematic illustration of the growth mechanism of Au nanoframes. $Ag^+$ and $Br^-$ ions show a synergistic function to obtain Au nanoframes.

To further investigate the etching effect, we choose to use Au nanoplates with the thickness of about 20 nm, which is realized by using 125 μM $AgNO_3$, as their etching is thorough but in a mild and controllable way. We find the etching initiates from the surface of Au nanoplates. As identified from Figures 3.1(d) and (e), crystallographic basal plane of the surface is Au (111). Previous studies show that $Br^-$ ions preferentially adsorb on Au (111), causing the unbalanced aggregation of $Br^-$ ions on Au (111) facets[35]. Meanwhile, it is well established that Au (111) facets possess planar defects such as stacking faults and twin boundaries, which result in the occurrence of the theoretically forbidden 1/3 (422) spots (Figure 3.1(d))[34]. Moreover, Au nanocrystals are observed to be unstable in the solution containing the halogen ions[30,35]. Thus, it is reasonable to speculate that $Br^-$ would favourably react with gold atoms on (111) planes given all the factors mentioned above. Aided by the oxygen solvated in the solution, the reaction can be listed as the following[27]:

$$O_2 + 2H_2O + 4e^- \longrightarrow 4OH^-$$
$$Au + 4Br^- \longrightarrow AuBr_4^- + 3e^-$$

Moreover, the edges of the nanoplate composed of (111) and (110) are occasionally found to be etched (Figure S3.4), indicating the etching process is not completely selective but preferable to a great extent. To verify such a role of $Br^-$ in the etching, we use the same amount of $I^-$ to replace $Br^-$ in the solution. As a consequence, we observe over-etched Au nanoplates (Figure S3.5) as $I^-$ is stronger than $Br^-$ as an etchant.

The synthesized Au nanoplates and Au nanoframes usually show aggregated morphology, which is undesirable for many applications, such as surface-enhanced Raman scattering (SERS). For instance, it is demonstrated that aggregation of Au nanoframes reduces, rather than increases, SERS effect due to the compromise of the inter- and intra-particle plasmonic fields[41]. To address this concern, we introduce the graphene multilayers in the solution and ultimately obtain graphene/Au nanoframes with improved dispersion, as shown in Figures 3.5(a) and (b). Besides, characterizations from XRD, SEM/EDX, and high-resolution TEM (Figures 3.5(c)-(i)) show that there are no changes in the crystalline orientations, atomic structures or element compositions of Au nanoframes when they are synthesized with graphene template. The improved dispersion is attributed to the presence of anchoring sites on graphene multilayers, which could immobilize Au nanocrystals from the nucleation stage and make the ultimate dispersion more homogenous[35,42].

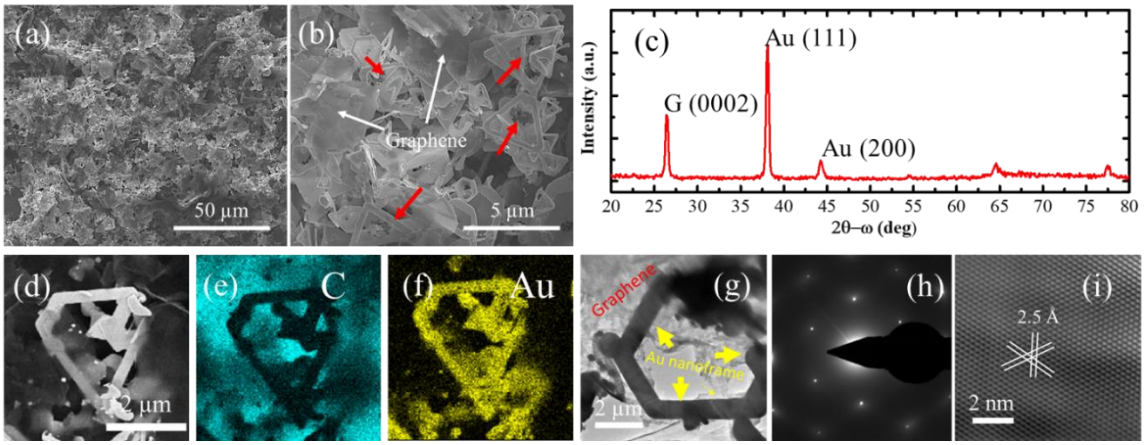


Figure 3. 5 Characterization of graphene grafted Au nanoframes. (a) Low and (b) high magnification SEM images of graphene supported Au nanoframes. Graphene and Au nanoframes are highlighted by white and red arrows, respectively in (b),

showing the improved dispersion of Au nanoframes. (c) 2θ-ω XRD scan of graphene/Au nanoframes. (d)-(f) EDX mapping of graphene/Au nanoframes with elements of C and Au captured. (g) A representative TEM image of Au nanoframes on graphene and (g) its selected area electron diffraction (SAED). (i) Atomic structure of Au nanoframes on the graphene template.

We now evaluate the SERS efficiency of the hybrid graphene/Au nanoframes platform. Prior to the measurement, we simulate the localized electrical field distributions around individual Au nanoframe in both triangular and hexagonal shapes. As illustrated in Figure 3.6(a), hot-spot regions of non-hollow Au nanoplates are limited in the tip area with extremely low intensity. On the other hand, hot-spot density is significantly higher in Au nanoframes as they are accumulated in areas along all the edges benefit from the hollow feature. As a consequence, the electrical field simulated from the frame is magnified significantly, which can enhance the Raman intensity by approximately $(E/E_0)^4$. We perform the Raman mapping of two different substrates (graphene/Au nanoframes vs. graphene/ Au nanoplates) decorated with $10^{-8}$ M R6G and find dramatically high density of hotspots from the platform with Au nanoframes, as shown in Figures 3.6(b) and (c). Therefore, we are able to detect the analyte, i.e. R6G at a concentration as low as $10^{-9}$ M using graphene/Au nanoframes as the SERS substrate (Figure 3.6(d)). Five signature peaks of the analyte at $10^{-9}$ M can be still clearly detectable at 1182, 1306, 1362, 1506, and 1647 $cm^{-1}$ [31]. This SERS platform demonstrates outstanding

reproducibility as well, as we are capable of probing R6G at $10^{-9}$ M from arbitrarily selected nine spots containing Au nanoframes on the substrate (Figure 3.6(e)).

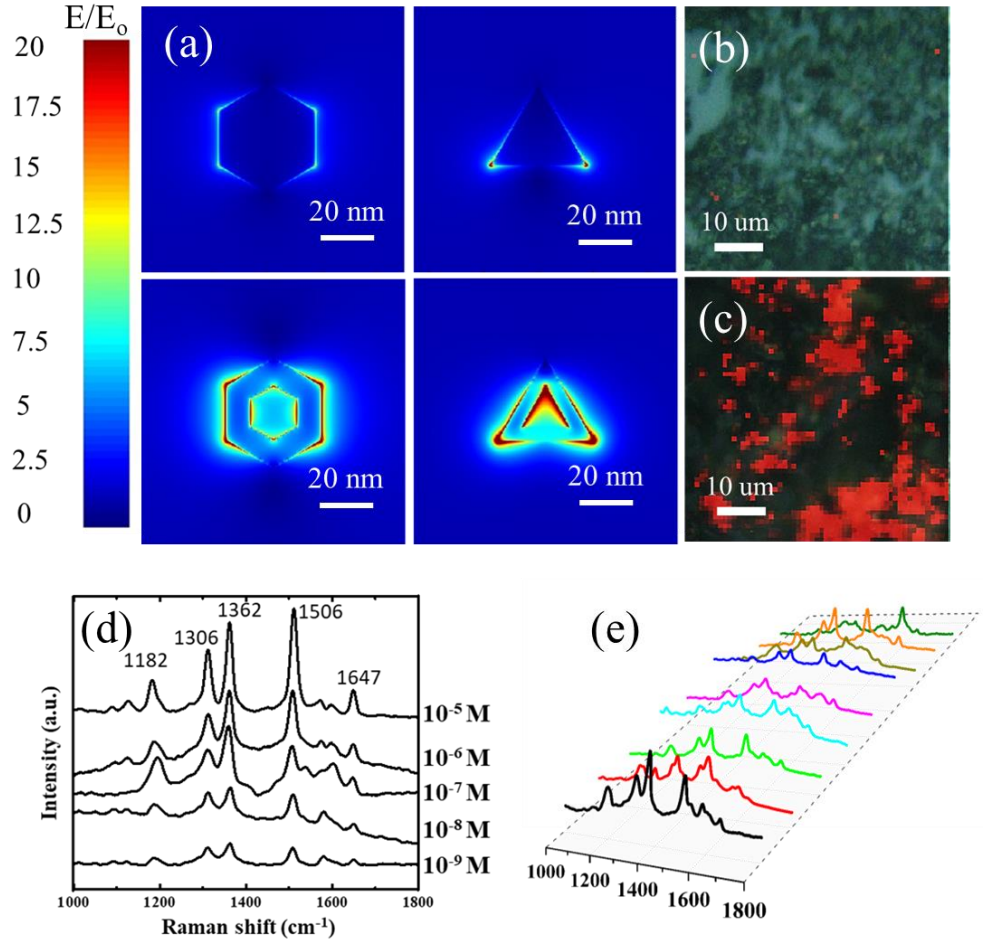


Figure 3. 6 (a) Simulation of localized electrical field enhancement of Au nanoplates and Au nanoframes. Raman hotspot mapping from the hybrid substrates of (b) graphene /Au nanoplates and (c) graphene/Au nanoframes with $10^{-8}$ M analyte. (d) SERS detection of R6G at the concentration from $10^{-5}$ to $10^{-9}$ M using graphene/Au nanoframes hybrid platform. (e) Evaluation of SERS reproducibility from nine arbitrarily selected spots.

When aggregated Au nanoframes (without graphene) are used as the SERS substrate, the detection limit of the analyte is $10^{-7}$ M (Figure S3.6). Their SERS sensitivity is quite close to those gained from Au nanoplates substrate.[31] Therefore, the detection limit from graphene/Au nanoframes is enhanced by two orders of magnitude compared with those substrates made of Au nanoframes and nanoplates. It has been reported graphene layers have shown multiple effects on SERS activities of plasmonic nanocrystals. First, there is the charge transfer between plasmonic Au nanostructures and graphene substrates[33,43]. The charge transfer contributes to the chemical enhancement (CM). Although weak, CM is one of the mechanisms responsible for the enhanced Raman scattering. The other mechanism is the electromagnetic enhancement (EM) that leads to the significant enhancement of localized surface plasmonic resonance (LSPR)[31,44]. Second, molecules of the analyte can have a more well-defined interaction with the hybrid SERS substrate due to the presence of oxygen-containing functional species on the graphene template. This will also improve the SERS performance[45]. Third, the benefit in terms of plasmonic activities from the unique hollow nanostructures disappears when Au nanoframes aggregates into an assembled entity, because there is actually no difference between aggregated Au nanoframes and Au nanoplates. It is demonstrated that aggregation of Au nanoframes reduces, rather than increases, SERS effect due to the compromise of the inter- and intra-particle plasmonic fields[41]. The dispersion of Au nanoframes is dramatically improved when graphene is introduced to the synthesis in this work. Accordingly, graphene template greatly enhances the SERS performance of Au nanoframes in our study.

## 3.4 Conclusions

In summary, we demonstrate a facile one-pot route to synthesize Au nanoframes by the etching of self-templates. We demonstrate pivotal roles of both $Ag^+$ and $Br^-$ ions in obtaining Au nanoframes. In addition, graphene template effectively improves the aggregation issue of Au nanoframes and the hybridized graphene/Au nanoframes substrate exhibits high SERS sensitivity that is capable of probing the analyte down to $10^{-9}$ M. Our approach greatly simplifies the tedious synthesis processes of Au nanoframes and proves the feasibility of synthesizing metallic nanoframes by etching self-templated nanoplates/nanosheets. This work may bring new insights to the synthesis of dimension-controllable Au nanocrystals and inspire the development of novel graphene-based nanocomposites.

3.5 References

1. Wang, X.; Feng, J.; Bai, Y.; Zhang, Q.; Yin, Y., Synthesis, Properties, and Applications of Hollow Micro-/Nanostructures. *Chem Rev* 2016, *116* (18), 10983-1060.

2. Zhang, Q.; Wang, W.; Goebl, J.; Yin, Y., Self-templated synthesis of hollow nanostructures. *Nano Today* 2009, *4* (6), 494-507.

3. Bolinger, P.-Y.; Stamou, D.; Vogel, H., Integrated nanoreactor systems: triggering the release and mixing of compounds inside single vesicles. *Journal of the American Chemical Society* 2004, *126* (28), 8594-8595.

4. Lee, J.; Park, J. C.; Song, H., A Nanoreactor Framework of a Au@SiO2 Yolk/Shell Structure for Catalytic Reduction ofp-Nitrophenol. *Advanced Materials* 2008, *20* (8), 1523-1528.

5. Luo, S.; Tang, M.; Shen, P. K.; Ye, S., Atomic-Scale Preparation of Octopod Nanoframes with High-Index Facets as Highly Active and Stable Catalysts. *Adv Mater* 2017, *29* (8).

6. Xu, X.; Zhang, Z.; Wang, X., Well-Defined Metal-Organic-Framework Hollow Nanostructures for Catalytic Reactions Involving Gases. *Adv Mater* 2015, *27* (36), 5365-71.

7. Mahmoud, M. A.; O'Neil, D.; El-Sayed, M. A., Hollow and Solid Metallic Nanoparticles in Sensing and in Nanocatalysis. *Chemistry of Materials* 2013, *26* (1), 44-58.

8. Ho, C.-C.; Zhao, K.; Lee, T.-Y., Quasi-3D gold nanoring cavity arrays with high-density hot-spots for SERS applications via nanosphere lithography. *Nanoscale* 2014, *6* (15), 8606-8611.

9. Kong, X. Y.; Ding, Y.; Yang, R.; Wang, Z. L., Single-crystal nanorings formed by epitaxial self-coiling of polar nanobelts. *Science* 2004, *303* (5662), 1348-1351.

10. Deng, Y.; Li, D.; Ning, X.; Zhang, D.; Zhang, S.; Zhang, Z.; Shan, D.; Wang, Z.; Liu, D.; Mao, X., Self-Assembly of Biocompatible FeSe Hollow Nanostructures and 2D CuFeSe Nanosheets with One-and Two-Photon Luminescence Properties. *Small* 2019, 1900627.

11. Métraux, G. S.; Cao, Y. C.; Jin, R.; Mirkin, C. A., Triangular nanoframes made of gold and silver. *Nano Letters* 2003, *3* (4), 519-522.

12. Xia, X.; Wang, Y.; Ruditskiy, A.; Xia, Y., 25th anniversary article: galvanic replacement: a simple and versatile route to hollow nanostructures with tunable and well-controlled properties. *Adv Mater* 2013, *25* (44), 6313-33.

13. Aherne, D.; Gara, M.; Kelly, J. M.; Gun'ko, Y. K., From Ag Nanoprisms to Triangular AuAg Nanoboxes. *Advanced Functional Materials* 2010, *20* (8), 1329-1338.

14. Shahjamali, M. M.; Bosman, M.; Cao, S.; Huang, X.; Cao, X.; Zhang, H.; Pramana, S. S.; Xue, C., Surfactant-free sub-2 nm ultrathin triangular gold nanoframes. *Small* 2013, *9* (17), 2880-6.

15. McEachran, M.; Keogh, D.; Pietrobon, B.; Cathcart, N.; Gourevich, I.; Coombs, N.; Kitaev, V., Ultrathin gold nanoframes through surfactant-free templating of faceted pentagonal silver nanoparticles. *J Am Chem Soc* 2011, *133* (21), 8066-9.

16. Lin, X.; Liu, Y.; Lin, M.; Zhang, Q.; Nie, Z., Synthesis of circular and triangular gold nanorings with tunable optical properties. *Chem Commun (Camb)* 2017, *53* (78), 10765-10767.

17. Jang, H.-J.; Hong, S.; Park, S., Shape-controlled synthesis of Pt nanoframes. *Journal of Materials Chemistry* 2012, *22* (37), 19792.

18. Wang, Z.; Wang, H.; Zhang, Z.; Yang, G.; He, T.; Yin, Y.; Jin, M., Synthesis of Pd Nanoframes by Excavating Solid Nanocrystals for Enhanced Catalytic Properties. *ACS Nano* 2017, *11* (1), 163-170.

19. Wu, Y.; Wang, D.; Zhou, G.; Yu, R.; Chen, C.; Li, Y., Sophisticated construction of Au islands on Pt-Ni: an ideal trimetallic nanoframe catalyst. *J Am Chem Soc* 2014, *136* (33), 11594-7.

20. Yan, X.; Yu, S.; Tang, Y.; Sun, D.; Xu, L.; Xue, C., Triangular AgAu@Pt core-shell nanoframes with a dendritic Pt shell and enhanced electrocatalytic performance toward the methanol oxidation reaction. *Nanoscale* 2018, *10* (5), 2231-2235.

21. Ruditskiy, A.; Xia, Y., The Science and Art of Carving Metal Nanocrystals. *ACS Nano* 2017, *11* (1), 23-27.

22. Lu, Q.; Wang, A. L.; Cheng, H.; Gong, Y.; Yun, Q.; Yang, N.; Li, B.; Chen, B.; Zhang, Q.; Zong, Y., Synthesis of hierarchical 4H/fcc Ru nanotubes for highly efficient hydrogen evolution in alkaline media. *Small* 2018, *14* (30), 1801090.

23. Fang, Z.; Wang, Y.; Liu, C.; Chen, S.; Sang, W.; Wang, C.; Zeng, J., Rational design of metal nanoframes for catalysis and plasmonics. *Small* 2015, *11* (22), 2593-2605.

24. Gao, Y.; Li, Y.; Wang, Y.; Chen, Y.; Gu, J.; Zhao, W.; Ding, J.; Shi, J., Controlled synthesis of multilayered gold nanoshells for enhanced photothermal therapy and SERS detection. *Small* 2015, *11* (1), 77-83.

25. Zhang, Z.; Luo, Z.; Chen, B.; Wei, C.; Zhao, J.; Chen, J.; Zhang, X.; Lai, Z.; Fan, Z.; Tan, C.; Zhao, M.; Lu, Q.; Li, B.; Zong, Y.; Yan, C.; Wang, G.; Xu, Z. J.; Zhang, H.,

One-Pot Synthesis of Highly Anisotropic Five-Fold-Twinned PtCu Nanoframes Used as a Bifunctional Electrocatalyst for Oxygen Reduction and Methanol Oxidation. *Adv Mater* 2016, *28* (39), 8712-8717.

26. Tsuji, M.; Hamasaki, M.; Yajima, A.; Hattori, M.; Tsuji, T.; Kawazumi, H., Synthesis of Pt–Ag alloy triangular nanoframes by galvanic replacement reactions followed by saturated NaCl treatment in an aqueous solution. *Materials Letters* 2014, *121*, 113-117.

27. Liu, H.; Yang, Q., Feasible synthesis of etched gold nanoplates with catalytic activity and SERS properties. *CrystEngComm* 2011, *13* (17), 5488.

28. Long, R.; Zhou, S.; Wiley, B. J.; Xiong, Y., Oxidative etching for controlled synthesis of metal nanocrystals: atomic addition and subtraction. *Chem Soc Rev* 2014, *43* (17), 6288-310.

29. Jang, H. J.; Ham, S.; Acapulco, J. A., Jr.; Song, Y.; Hong, S.; Shuford, K. L.; Park, S., Fabrication of 2D Au nanorings with Pt framework. *J Am Chem Soc* 2014, *136* (50), 17674-80.

30. Chen, L.; Ji, F.; Xu, Y.; He, L.; Mi, Y.; Bao, F.; Sun, B.; Zhang, X.; Zhang, Q., High-yield seedless synthesis of triangular gold nanoplates through oxidative etching. *Nano Lett* 2014, *14* (12), 7201-6.

31. Xin, W.; Yang, J. M.; Li, C.; Goorsky, M. S.; Carlson, L.; De Rosa, I. M., Novel Strategy for One-Pot Synthesis of Gold Nanoplates on Carbon Nanotube Sheet As an Effective Flexible SERS Substrate. *ACS Appl Mater Interfaces* 2017, *9* (7), 6246-6254.

32. Xin, W.; De Rosa, I. M.; Cao, Y.; Yin, X.; Yu, H.; Ye, P.; Carlson, L.; Yang, J. M., Ultrasonication-assisted synthesis of high aspect ratio gold nanowires on a graphene

template and investigation of their growth mechanism. *Chem Commun (Camb)* 2018, *54* (33), 4124-4127.

33. Xin, W.; De Rosa, I. M.; Ye, P.; Severino, J.; Li, C.; Yin, X.; Goorsky, M. S.; Carlson, L.; Yang, J. M., Graphene template-induced growth of single-crystalline gold nanobelts with high structural tunability. *Nanoscale* 2018, *10* (6), 2764-2773.

34. Jin, R.; Cao, Y.; Mirkin, C. A.; Kelly, K.; Schatz, G. C.; Zheng, J., Photoinduced conversion of silver nanospheres to nanoprisms. *science* 2001, *294* (5548), 1901-1903.

35. Xin, W.; Severino, J.; De Rosa, I. M.; Yu, D.; McKay, J.; Ye, P.; Yin, X.; Yang, J. M.; Carlson, L.; Kodambaka, S., One-Step Synthesis of Tunable-Size Gold Nanoplates on Graphene Multilayers. *Nano Lett* 2018, *18* (3), 1875-1881.

36. Liu, M.; Guyot-Sionnest, P., Mechanism of silver (I)-assisted growth of gold nanorods and bipyramids. *The Journal of Physical Chemistry B* 2005, *109* (47), 22192-22200.

37. Personick, M. L.; Langille, M. R.; Zhang, J.; Mirkin, C. A., Shape control of gold nanoparticles by silver underpotential deposition. *Nano Lett* 2011, *11* (8), 3394-8.

38. Qian, Z.; Park, S.-J., Silver Seeds and Aromatic Surfactants Facilitate the Growth of Anisotropic Metal Nanoparticles: Gold Triangular Nanoprisms and Ultrathin Nanowires. *Chemistry of Materials* 2014, *26* (21), 6172-6177.

39. Moreau, L. M.; Jones, M. R.; Roth, E. W.; Wu, J.; Kewalramani, S.; O'Brien, M. N.; Chen, B. R.; Mirkin, C. A.; Bedzyk, M. J., The role of trace Ag in the synthesis of Au nanorods. *Nanoscale* 2019, *11* (24), 11744-11754.

40. Murphy, C. J.; Thompson, L. B.; Alkilany, A. M.; Sisco, P. N.; Boulos, S. P.; Sivapalan, S. T.; Yang, J. A.; Chernak, D. J.; Huang, J., The many faces of gold nanorods. *The Journal of Physical Chemistry Letters* 2010, *1* (19), 2867-2875.

41. Mahmoud, M.; El-Sayed, M., Aggregation of gold nanoframes reduces, rather than enhances, SERS efficiency due to the trade-off of the inter-and intraparticle plasmonic fields. *Nano letters* 2009, *9* (8), 3025-3031.

42. Xin, W.; De Rosa, I. M.; Ye, P.; Zheng, L.; Cao, Y.; Cao, C.; Carlson, L.; Yang, J.-M., Simplified Fabrication Strategy of Graphene Liquid Cells for the in Situ Transmission Electron Microscopy Study of Au Nanoparticles. *The Journal of Physical Chemistry C* 2019, *123* (7), 4523-4530.

43. Wang, P.; Liang, O.; Zhang, W.; Schroeder, T.; Xie, Y.H., Ultra-sensitive graphene-plasmonic hybrid platform for label-free detection. *Advanced Materials*, 2013 *25*(35), 4918-4924.

44. Stiles, P.L.; Dieringer, J.A.; Shah, N.C.; Van Duyne, R.P., Surface-enhanced Raman spectroscopy. *Annu. Rev. Anal. Chem.*, 2008 *1*, 601-626.

45. Murphy, S.; Huang, L.; Kamat, P.V., Reduced graphene oxide–silver nanoparticle composite as an active SERS material. *The Journal of Physical Chemistry C*, 2013 *117*(9), 4740-4747.

3.6 Supplementary Information

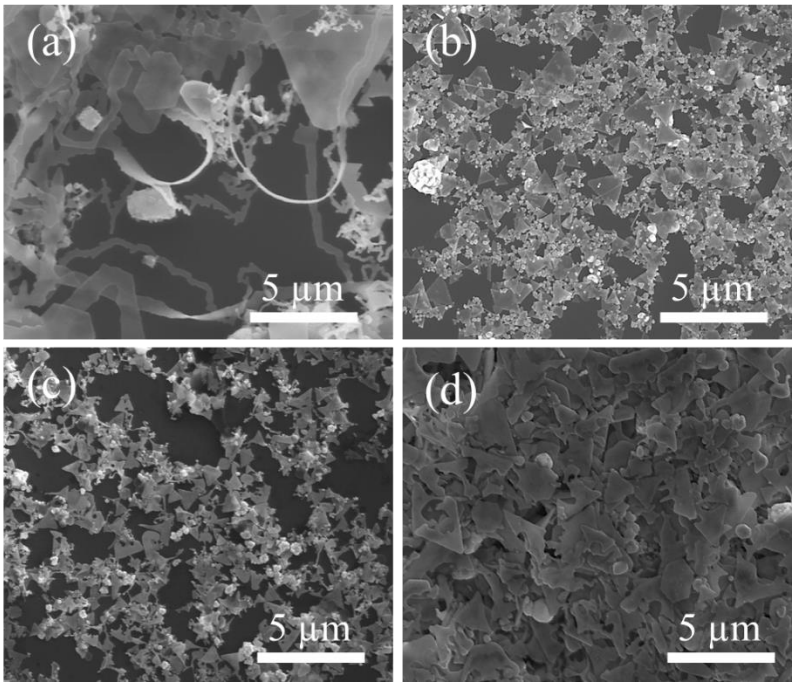


Figure S3. 1 Samples synthesized with different amount of KBr. (a) 0 µL. (b) 15 µM. (c) 300 µM. (d) 750 µM.

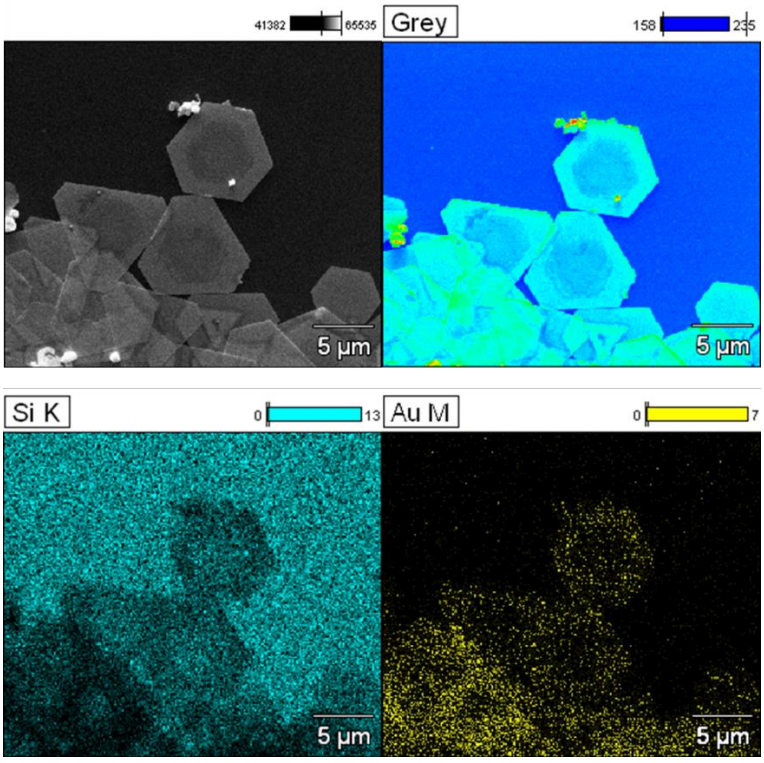


Figure S3. 2 EDX mapping of Au nanoplates aged at 24 hrs.

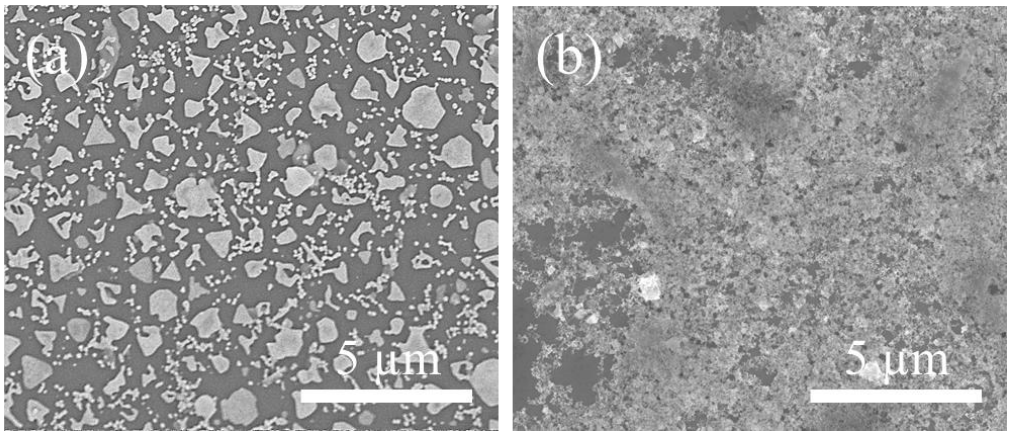


Figure S3. 3 Au nanocrystals synthesized in the standard condition (80 $^{o}$C 1hr and aged for 4 hrs at room temperature) with different amount of $AgNO_3$ solution. (a) 10 μM $AgNO_3$. (b) 800 μM $AgNO_3$.

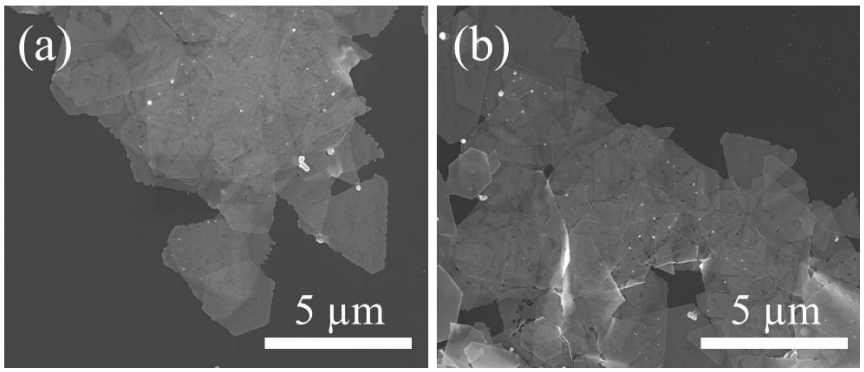


Figure S3. 4 Examples of Au nanoplates with the etched edges synthesized in the standard condition and aged for 24 hrs.

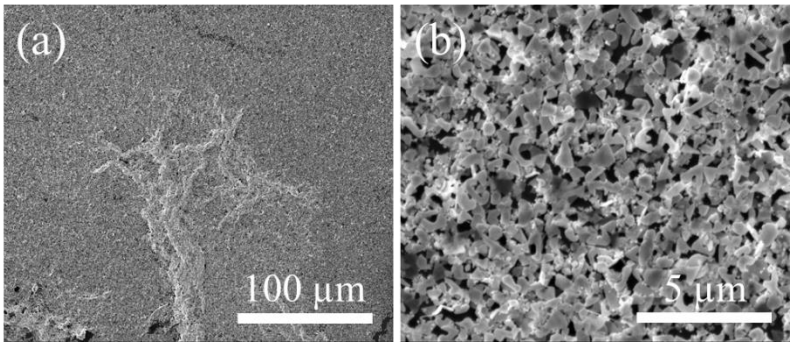


Figure S3. 5 Au nanocrystals synthesized in the standard method and aged for 48 hrs except that the same amount of KI was used to replace KBr. Au nanoplates was not observed owing the stronger etching effect from $I^-$ ions than $Br^-$ ions.

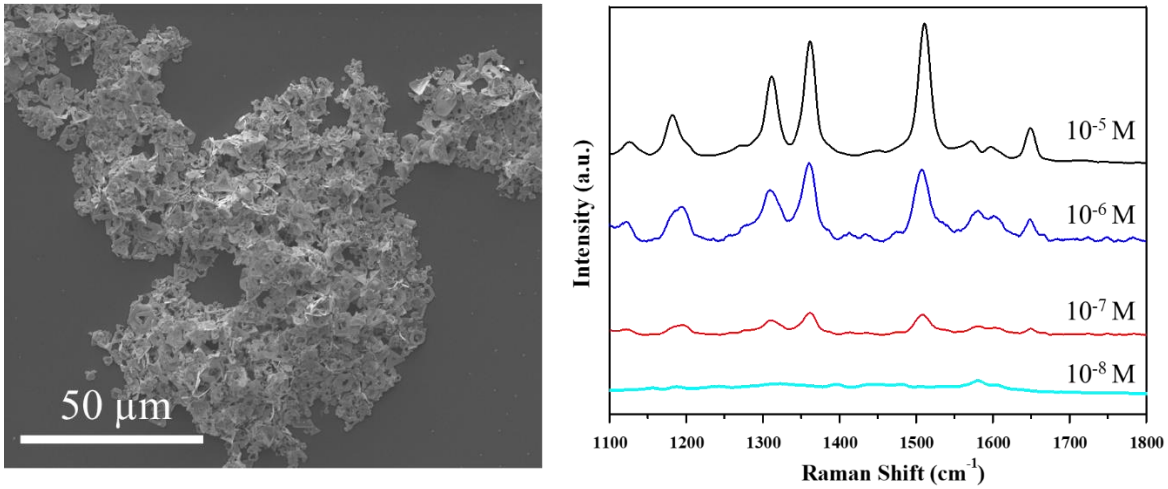


Figure S3. 6 SERS substrate made from the aggregated Au nanoframes without graphene template and the Raman scattering of R6G using this substrate.

# Chapter 4 Single-Layer $MoS_2$ Based Au Gap Plasmon Enhanced Photoelectrochemical Cells for Efficient Water Splitting

## Abstract

Metal nanoparticles and metal film coupling (Gap Plasmon) have been shown to possess distinguished plasmonic properties compared with other nano-metallic structures, the enhanced electric field is extremely localized within the narrow gap region when the gap thickness reaches 10 nm or less. The field enhancement is known to be inversely proportional to the gap thickness. Hence reducing the gap thickness is important to achieve the highest possible field enhancement. In this work, it is demonstrated for the first time that using single-layer $MoS_2$ as a well-defined nanospacer between Au-nanoparticles (AuNPs) and Au-film, which could offer an extremely high localized electric field enhancement within the gap. The $MoS_2$ Raman intensity with the Surface Enhanced Raman Scattering (SERS) enhancement factor (EF) up to $5x10^6$ is obtained from the $MoS_2$-Au gap plasmon system. A 5-fold increase in the photocurrent is obtained from the $MoS_2$-Au gap plasmon as the working electrode compared to that from bare $MoS_2$ prepared under the same condition. Compared with individual metal nanoparticles commonly used to enhance thin-film photocatalytic process, gap-plasmon could theoretically produce 8 orders of magnitude higher SERS EF and precise control the hot spot location to superimpose where ultrathin materials locate thus using the higher incident energy available.

## 4.1 Introduction

$H_2$ has long been known to be one of the highest energy density fuels[1] with water as the only by product. Fuel cell technology has been actively pursued as an environmentally friendly power source for automobiles[2]. The promise of the technology is hindered by the lacking of a sustainable way of producing $H_2$. Solar water-splitting via photo-electrochemical cells (PEC)[3] is the most promising approach with intense research effort being dedicated to it[4-6]. One bottleneck commonly identified for solar water splitting is the limited charge carrier diffusion length inside the semiconductor, typically below 20 nm[7], electron and hole pairs that created inside the bulk semiconductor can hardly diffuse out to the surface which in result cannot contribute to the overall water splitting. Therefore, thin layers of semiconductors are very much preferred to increase the yield of hydrogen production[7].

Another important factor for a semiconductor to be an effective PEC cell is its bandgap. The energy bands of the semiconductor (conduction band and valence band) need to be properly aligned with the redox potentials of water, with the energy bandgap ($E_g$) being larger than the potential difference between the reduction of $H_2$ and the production of $O_2$. In the meantime, the $E_g$ needs to be sufficiently small in order to absorb much of the solar radiation available[3]. The preferred $E_g$ range for PEC cell is typically reported to be between 1.6 ev to 2.4 ev[8-9]. To date, only a handful of semiconductor materials meet the requirement with the energy bands that being properly aligned with the redox potentials of water, such as $BiVO_4$[10], GaP[11], $TiO_2$[12-14], $Cu_2O$[15], single-layer $MoS_2$[16-17] etc. Among them, single-layer $MoS_2$ possesses the correct chemical over-potential while with the bulk form $MoS_2$ having $E_g$ values too small for the intended purpose[18]. Moreover, $MoS_2$ is an earth-abundant,

chemically stable, non-toxic material, which make it a perfect candidate for the photoelectrodes. However, single-layer $MoS_2$ still facing the problem of limited optical absorption cross-section due to the extreme thin property. Herein, it is demonstrated for the first time single-layer $MoS_2$ packed between AuNPs and Au film (referred $MoS_2$-Au gap plasmon system), where extremely high electric field (hot spots) locates, similar gap plasmon structure studies have already demonstrated that gap thickness here plays a significant role on the electric field enhancement inside gap, the field enhancement is known to be inversely proportional to the gap thickness[19]. Hence reducing the gap thickness is important to achieve the highest possible field enhancement with gap thickness decreases. Considering the single-layer $MoS_2$ is the thinnest $MoS_2$ space layer that can be ever prepared, it is expected that using it as a well-defined sub-nanometer space layer will significantly enhance electric field within the gap. Though some studies have been done for plasmon enhanced single-layer $MoS_2$ water splitting from individual AuNPs[16, 21], no previous report have been focused on the enhanced $MoS_2$ photocatalysis from the gap plasmon system that using single layer $MoS_2$ as the space layer inside the gap where much higher field intensity is available.

This gap plasmon structure, is not limited to $MoS_2$ but can easily be extended to other single-layer Van der Waals materials such as graphene, black phosphorus, hBN. Within the sub-nanometer thick gap plasmon structure, those significantly enhanced field intensity could enables a variety of interesting applications, such as surface-enhanced Raman scattering[22].

## 4.2 Experimental

### 4.2.1 Sample Preparation.

Synthesis of Single-layer $MoS_2$: We used reported chemical vapor deposition methods to grow $MoS_2$ on 300nm $SiO_2$ sheet substrate[23]. The equipment setup is schematically shown in Figure S4.1, the typical single-layer $MoS_2$ morphology and single-layer $MoS_2$ surface converge shown in Figure S4.1 inset. In brief, 10 mg $MoO_3$ powder and 500 mg S powder were used as Mo and S precursors, respectively. The 300nm $SiO_2$ substrate was put up-side down facing towards the $MoO_3$ powder localized at the furnace centre. The substrate temperature is set to be 850 $^oC$, while sulfur powder was put at the temperature window, where the temperature was set as 200 $^oC$. The total growth time was 15min. During the growth, Ar was employed as the carrier gas with a flow rate of 100 sccm. The thickness of as-grown $MoS_2$ space layers before the transfer is measured via atomic force microscopy (AFM) images which is shown as shown in figure S4.2. The obtained average thickness is about 0.7nm, which corresponded with single layer $MoS_2$ thickness[20].

Synthesis of Au nanoparticles: Gold chloride hydrate (HAuCl4·xH2O, 99.999% purity) and polyethyleneimine (PEI, branched, average molecular weight Mw ~25,000) are purchased from Sigma-Aldrich, USA. The chemicals are used without any further treatment or purification. The similar method reported in chapter 3 is adopted to synthesis AuNPs[24]. First, 220 mg of aqueous PEI solution (27 mg/mL) is mixed with 20 mL of deionized water in a glass vial. Then, 35 µL of 40 mM $HAuCl_4$ solution is added and gently shaken for 1 minute. The glass vial is then capped and kept at 80 oC in the oven for hydrothermal reduction of gold precursor for 1 hr. PEI serves as the reducing agent as well as the stabilizer for Au nanoparticles in this standard synthesis procedure. At t = 0, the

solution appears light yellow and after 15 min, the color of the solution gradually changed to wine red. After completion of the reaction, the product, i.e. AuNPs, are used later.

Fabrication the $MoS_2$-Au Gap Plasmon System: The 50 nm gold film was deposited on Si substrate via very slow electron-beam evaporate rate (0.1A $s^{-1}$) after depositing 5 nm thick chromium as adhesion layer. The as-grown single-layer $MoS_2$ film was transferred to gold film using the reported PMMA-assisted method[25]. The as synthesized Au nanoparticle was deposited on as prepared $MoS_2$-Au film substrate using a pipette. The hybrid substrate was dried in the vacuum oven at 100 $^oC$ for 2 hours. The deposition process was repeated by 3 times to assure the substrate was covered with enough AuNPs, the schematic of the $MoS_2$-Au gap plasmon system is shown in figure 4.1 (d). The control experiments were carried out with 4 slightly different configurations shown in figure 4.1 to better elucidate the performance of $MoS_2$-Au gap plasmon system

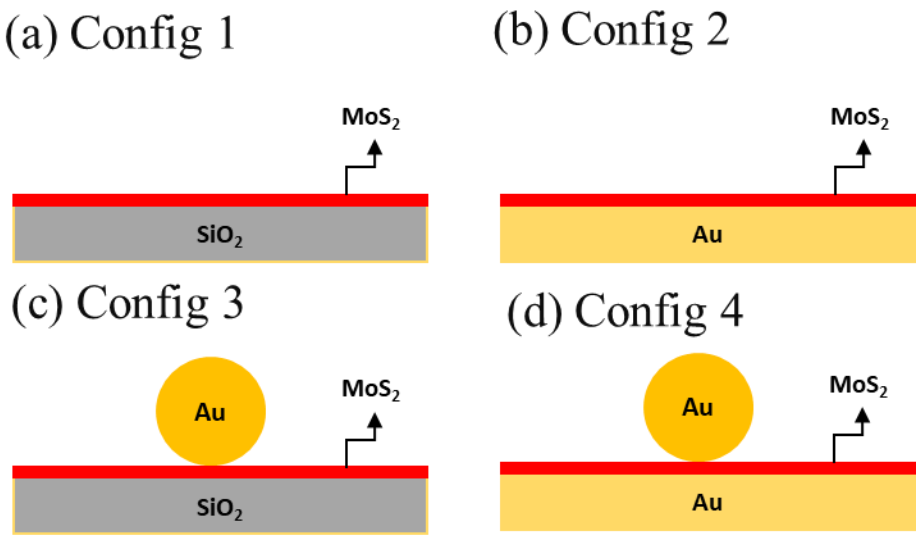


Figure 4. 1 (a) $MoS_2$ on $SiO_2$ substrate. (b) $MoS_2$ on Au film substrate. (c) $MoS_2$ on $SiO_2$ substrate with AuNPs. (d) $MoS_2$-Au gap plasmon system

Surface Enhanced Raman Scattering Measurements: Raman spectroscopy analysis was obtained with a Renishaw In-Via Raman system, the of 633 nm laser length with power of 1mW was used, the objective lens magnification of 50x and a grating spacing of 1200 *l*/mm was used, $MoS_2$ Raman spectra was acquired from 4 different configurations as the control experiments.

Photocurrent Measurements: A xenon light source was used; optical power is measured to around 300 $mW/cm^2$. To measure the photocurrent, a home-built electrochemical system with 3 electrodes configurations was used. $MoS_2$-Au gap plasmon system (config 4) is used as the working electrode, Ag/AgCl electrode as reference electrode and Pt as counter electrode. All potentials are reported against standard Ag/AgCl voltage. The electrolyte was aqueous 0.1 M $KH_2PO_4$ buffer at pH 7 with no additive. The voltammetry sweep was manual performed from 0 to 1.2 V at the step rate of 0.1v/sec immediately after the sample was fully immersed into the electrolyte. Two control experiments are carried out with $MoS_2$ on flat Au (config 2) and flat Au as the working electrode with rest setup remain the same.

FDTD Simulations: The near field electromagnetic field distribution was simulated via finite difference time domain simulation (Lumerical FDTD simulations). The perfect match layer (PML) was set as the absorptive boundary. The mesh size was set at 0.1 nm × 0.1 nm × 0.1 nm within the simulation area. The diameter of Au nanoparticles to was

appointed as 20 nm. the space layer of monolayer $MoS_2$ set as 1nm in thickness. The thickness of Au film underneath $MoS_2$ is set as 50 nm. The dielectric function of Au was obtained from Johnson and Christy[26]. The $MoS_2$ dielectric constant was taken from Laturia[27]. The simulation result shows the $E/E_0$ distribution along the top surface of $MoS_2$ as well as the side view of the structure. The extremely strong near-field produced in the proposed $MoS_2$-Au gap plasmon system (config 4) shown in Figure S4.4 which is due to couplings between the AuNPs and Au films[28]. The theoretical local SERS enhancement factor $(E/E_0)^4$ reaches up to $10^8$. Config 3 also shows some low near-field enhancement $(E/E_0)^4$ up to $10^3$ mainly from AuNPs itself[29], while config 1 and 2 didn't show enhanced field intensity near surface due to the non-metallic or flat surface under.

Characterizations: Top view scanning electron microscopy (SEM) images of samples were obtained with FEI Nova NanoSEM 230. Transmission electron microscopy (TEM) and high-resolution transmission electron microscopy (HRTEM) images were captured with FEI Titan S/TEM system at 60 keV. Raman spectra are measured using Renishaw inVia microscope under 633 nm laser excitation. The laser power used is ~1 mW. The grating used is 1800 l/mm and the objective lens used is 50x.

## 4.3 Results and Discussion

### 4.3.1 $MoS_2$-Au gap plasmon system

The $MoS_2$-Au gap plasmon system (Figure 1(d)) is made of a three-layer structure consisting of 20nm diameter AuNPs sitting on top of near continuous single-layer $MoS_2$

with another 50nm thick Au film on bottom Si substrate, low and high-magnification of SEM images are utilized to observe the surface morphology of different stages related to preparing $MoS_2$-Au gap plasmon system, three stages include the structure of very slowly deposited (0.1 A/sec) 50nm Au film (Figure 4.2 (a), (d)), transferred single-layer $MoS_2$ on 50nm Au film(Figure 4.2 (b), (e)), and finally $MoS_2$-Au gap plasmon system after AuNPs deposition(Figure 4.2 (c), (f)). The bare Au film is observed in figure 4.2 (a), (d), it is worth to mention that some surface roughness on the Au film is observed under high-magnification of SEM image shown in figure 4.2 (d), it is expect that surface roughness is contributed to the later slight enhanced Raman intensity from $MoS_2$. It is observed in figure 4.2 (b) that $MoS_2$ surface coverage on Au film to be more than 80% which is similar as the coverage before transfer. It is also clearly observed in figure 4.2 (d) the edge of single-layer $MoS_2$ resulting from the different surface morphology between $MoS_2$ and the uncovered Au film. The similar roughed morphology of Au film under $MoS_2$ can also be clearly observed due to the extremely thin property of the single-layer $MoS_2$. It is found in figure 4.2 (f) that the AuNPs deposited on $MoS_2$ could be clearly visualized especially on the $MoS_2$ films as $MoS_2$ is a well-proven diffusion barrier[16] which could avoid AuNPs to migrate through. The AuNPs can barely be visualized from Au film without placing single-layer $MoS_2$ film in between due to the metal migration. High coverage of single-layer $MoS_2$ on Au film significantly avoids subsequent deposited AuNPs migrating to the bottom Au film. The thickness of as-prepared $MoS_2$ space layers is measured via atomic force microscopy (AFM) images which shown in figure S4.2. The thickness obtained is about 0.7 nm, corresponded with single layer $MoS_2$ profile[20]. It confirms that the thinnest available $MoS_2$ as space layer in gap plasmon system is successfully being prepared. This

geometrically proves that single-layer $MoS_2$ could be effectively used as a well-defined spacer layer inside gap plasmon system. The AuNPs size and coverage is clearly visualized from HRTEM image in figure S4.3 (a). It is also obtained that the average AuNPs diameter is around 20 nm and the average separation distance between nearby AuNPs is around 7 nm, the corresponding statistic histogram of AuNPs size and separation distance is shown in figure S4.3 (b) and (c). The very high coverage of AuNPs is very beneficial to the entire $MoS_2$ surface to make full use of incident light above across the entire $MoS_2$ film.

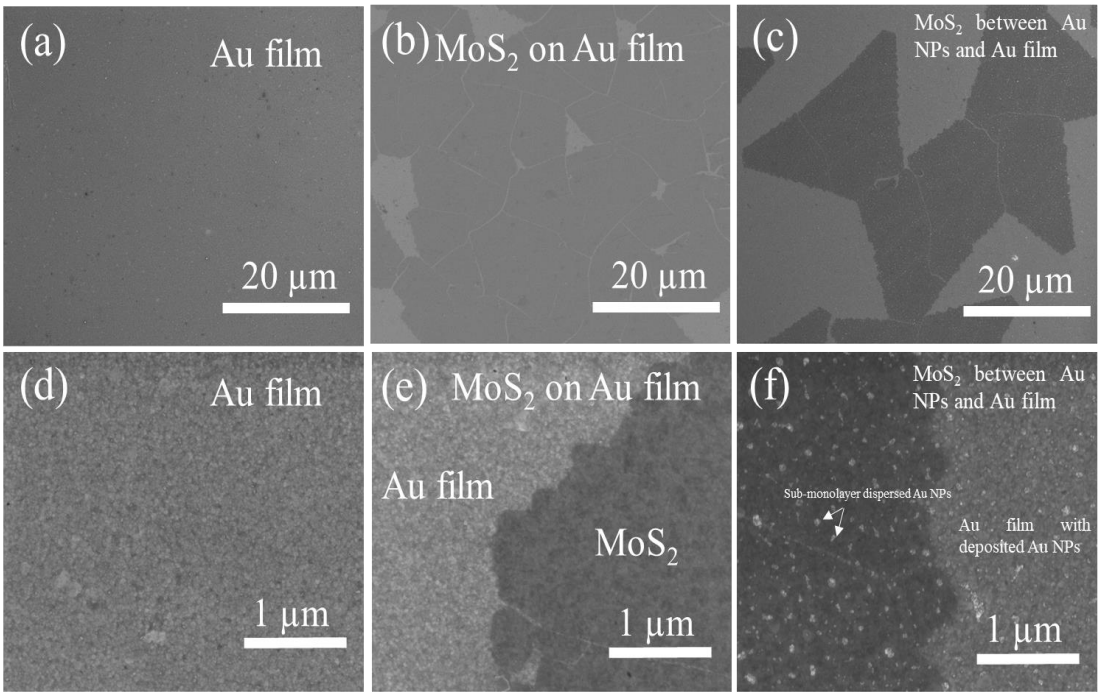


Figure 4. 2 Low-magnification of SEM images of structures used in (a) Au film (b) $MoS_2$ on Au film substrate. (c) $MoS_2$-Au gap plasmon system. High-magnification of SEM images of structures (d) a zoomed-in image of Au film. (e) a zoomed-in image of $MoS_2$ on Au film substrate. (f) a zoomed-in image of $MoS_2$-Au gap plasmon system.

It is shown in Figure 4.3 (a) the high-resolution TEM image of single-layer $MoS_2$ films after AuNPs were synthesized and deposited on. It is observed that many AuNPs packed on top of $MoS_2$ film. The lattice spacing of 2.7A with six-fold symmetry corresponds to the $MoS_2$ (100) plane[30] and the clear inter-planar spacing of 2.4A corresponds to Au (111) plane[24], respectively. These results are in agreement with the selected area electron diffraction (SEAD) pattern shown in Figure 4.3 (b). The diffraction spots can be divided into two categories, which are assigned to AuNPs and $MoS_2$ film correspond. The diffraction ring of Au (111) planes is observed as shown in yellow circle. The bright spots circled in white square can be indexed to (100) diffraction spots of $MoS_2$[30], respectively. Furthermore, the element distribution of Au-$MoS_2$ composite were investigated by energy-dispersive X-ray spectrometry (EDX) shown in Figure 4.3 c-f. The element Mo, S and Au distribution can be observed. It shows the co-existence of Mo, S and Au and relative uniform distribution along the selective area.

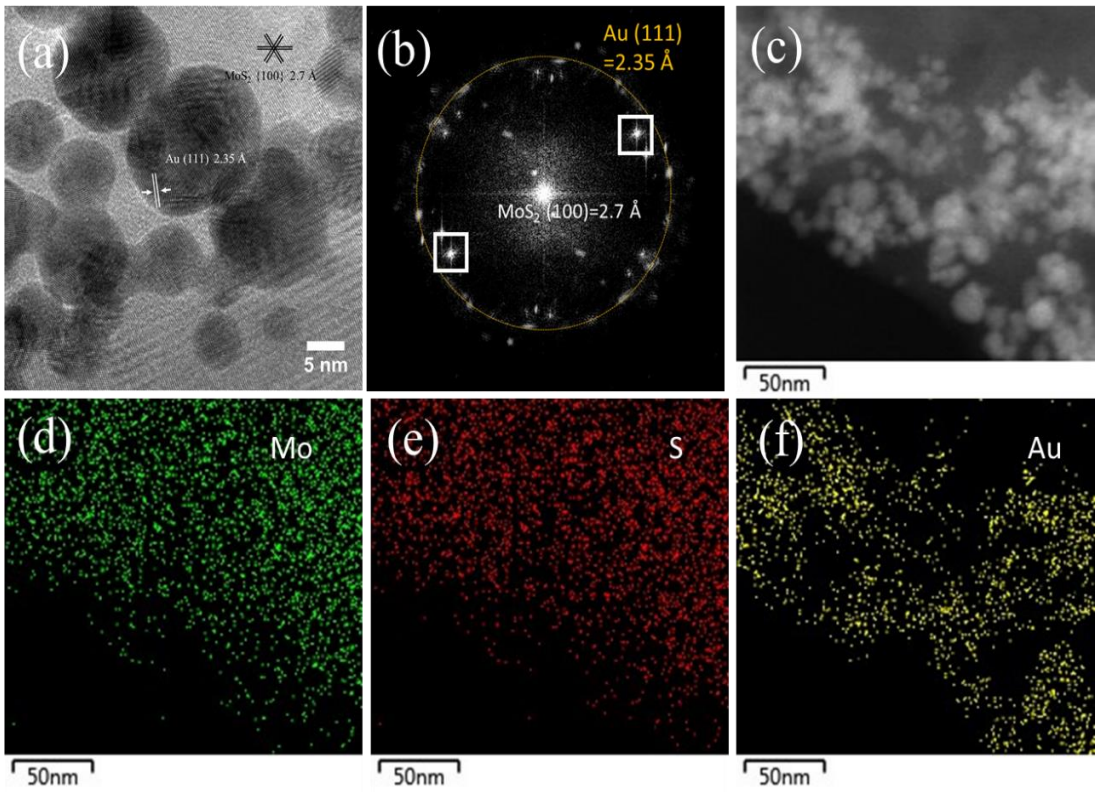


Figure 4. 3 (a) HRTEM image of AuNPs directly deposited on $MoS_2$, showing the distinguishable lattice parameter between Au and $MoS_2$. (b) the selected area electron diffraction (SEAD) pattern of $MoS_2$-Au compound (c) selected area TEM image (d) EDX mapping of Mo element (e)EDX mapping of S element (f) EDX mapping of Au element

4.3.2 Enhanced SERS in $MoS_2$-Au plasmon gap System

The field enhancement is first studied by detecting Raman intensity from $MoS_2$ from 4 different configurations shown in figure 4.1. Since Raman spectroscopy is a widely used tool to analysis the optical response towards monolayer $MoS_2$[31] and its SERS intensity directly correlates with the strength of the localized electrical field that is enhanced by the

surface plasmon from neighboring AuNPs or Au films[32-34], so $MoS_2$ Raman intensity is the best benchmark for investigating the near electrical field enhancement. The 633nm laser is used to for all the SERS measurement to match the plasmon resonance of the as-prepared AuNPs. As shown in figure 4.4, config 1 represent the typical Raman spectra for monolayer $MoS_2$ layer on $SiO_2$/Si with its 2 major peaks, $E_{2g}$ (385cm$^{-1}$) and $A_{1g}$(405cm$^{-1}$) can be identified but show a very low signal-to-noise ratio due to the typical low Raman activity, the $E_{2g}$ peak represents the vibration mode of Mo S atoms in the basal plane, whereas the $A_{1g}$ peak represents the S atoms out of plane vibration modes. Here, 20cm$^{-1}$ Raman shift difference between $A_{1g}$ and $E_{2g}$ confirms the single-layer $MoS_2$ property[31], this finding corresponds with our AFM result before. Another 460 cm$^{-1}$ can also be distinguishable which is original from the LA and LA' photon at the M point[35], apart from these, no other $MoS_2$ related peak can be observed from config 1. Raman intensity of the $MoS_2$ from Config 2, 3, 4 all show various enhanced intensity compared to normal Raman spectra from config 1, it can be clearly seen that S/N ratios of Raman spectra from config 3 and 4 are much higher than those from config 1 and 2 mostly due to surface plasmon coupling between neighboring nano units, this finding corresponds with our FDTD simulation results before (Figure S4.4). The spectra from config 4 shows the most enriched spectral information as expected due to the extremely strong surface plasmon resonance from gap plasmon system. The newly exposed peaks at 528 cm$^{-1}$, 573 cm$^{-1}$ and 645cm$^{-1}$ are assigned to $MoS_2$ $E_g$(M)+TA'(M), $A_{1g}$(M)+TA'(M), and $A_{1g}$(M)+LA'(M)[35], respectively. The spectra from config 3 shows some enhancement due to the partilly resonace from neighboring AuNPs as was confirmed simulation result in figure S4.4c. The sepctra from config 2 shows slight enhancement possibly due to the factor the as-prepared Au film is

not atomiclly flat which renders some surface plasmoc resonance towards the $MoS_2$ layer on top.

To quantitatively describe the spectra enhacement, SERS enhancemcemnt factors (EF) are adopted as a figure of merit to represent the boosted raman signal, we employ the following equation:

$$EF = (I_{SERS} \times A_{Raman}) / (I_{Raman} \times A_{hotspot})$$

where $I_{SERS}$ and $I_{Raman}$ represent the SERS and normal Raman intensities of the analyte acquired under identical conditions. $A_{Raman}$ is the area of the laser excitation spot on flat region. We used 50× lens with NA 0.55 for 633 nm laser, and the calculated laser spot size is ~1400nm[35]. We take $A_{Raman}$ as a 1400×1400 nm area and take $A_{hotspot}$ as a 10×10 nm area. The SERS EF for $A_{1g}$ band of $MoS_2$ is calculated to be ~ $4x10^5$ and ~$9x10^5$ for config 2 and config 3 as to normal Raman from config 1, respectively. Remarkably, For the $MoS_2$-Au gap plasmon system (config 4), the typical SERS EF is about ~$5x10^6$ compared with normal Raman from config 1, this enhanced ratio is significantly higher than just simple linear superposition from two separate structure with $MoS_2$, i.e. Au film under $MoS_2$ (SPP from the Au film) and AuNPs on $MoS_2$ (LSP from the AuNPs). The significant enhancement is promoted due to the strong plasmonic couplings between the AuNP-Au film coupling with only 0.7nm thick single-layer $MoS_2$ as the space layer. It should be mentioned, to our best knowledge, it is first time surface enhanced Raman study on gap plasmon system with single-layer $MoS_2$ as the spacer layer that is ever been reported and it is one of highest SERS EF ever reported so far for plasmon-enhanced $MoS_2$[35-37].

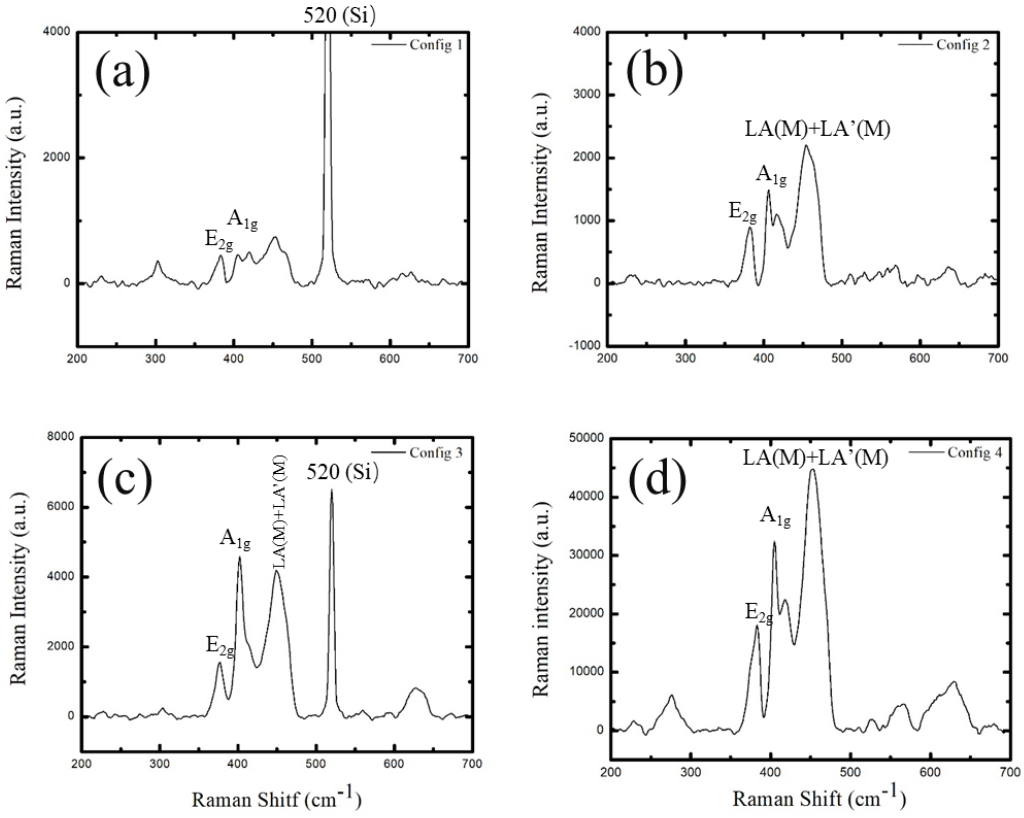


Figure 4. 4 (a) Normal Raman spectra of $MoS_2$ from config 1. (b) SERS spectra of MoS2 on Au film from config 2. (c) SERS spectra of $MoS_2$ with AuNPs deposited on top from config 3. (d) $MoS_2$-Au gap plasmon system from config 4. The excitation wavelength is 633 nm.

### 4.3.3 Photocurrent Measurements

It is illustrated in Figure 4.5 (a), the electron hole pairs are generated when shining the light towards working electrode. The generated electrons were transferred from the Au-$MoS_2$ working electrode through the Au substrate towards the counter electrode Pt, where hydrogen ion was reduced to generate hydrogen gas. On the working electrode, the left

behind holes on the Au-$MoS_2$ surface oxidize water molecules to generate oxygen. The linear sweep voltammograms show that the working electrode made from config 2 (pure $MoS_2$ on Au film) exhibited a photocurrent of 110 $\mu A/cm^2$ at 0.8 V under visible light illumination (Figure 4.5 (b)) similar to the previous reported monolayer $MoS_2$ on FTO substrate photocurrent values[38]. The same measurement is carried out using config 4 as working electrode ($MoS_2$-Au gap plasmon system), with the gap plasmon resonance within the $MoS_2$ the photocurrent can boost the photocurrent up to 590 $\mu A/cm^2$ at 0.8 V (Figure 4.5 (b)), a 5-fold increase in photocurrent has been achieved for gap plasmon system. Here the gap plasmon system plays a few important roles here, first, AuNPs coupling with the Au film separated by only single-layer $MoS_2$ distance generates an extremely high localized electric field(Figure S4.4 (d)), which facilitate more electron-hole pairs generation and separation in $MoS_2$[38]. Second, Au films severs as the electron sink to trap the generated electron move away from $MoS_2$ and to the counter electrode[39], third, AuNPs as a hot plasmon-excited electrons provider for the direct water reduction towards the counter electrode[39-42]. The switched ON and OFF photocurrent of working electrodes made from config 2 and 4 is shown in Figure 4.5 (c). It is observed that when light is on, the photocurrent increases immediately, and the on photocurrent is significantly larger than when the light is off, the on and off ratio reaches to about 100 when using config 4 (gap plasmon) as the working electrode. These results show that single-layer $MoS_2$ thin film exhibits extreme sensitive towards photo activity, the normalized-on photocurrent ratio from config 4 and config 2 is around 5, which is consistent with the photocurrent from config 4 and config 2 when potential vs Ag/AgCl is at 0.8v in Figure 4.5 (b).

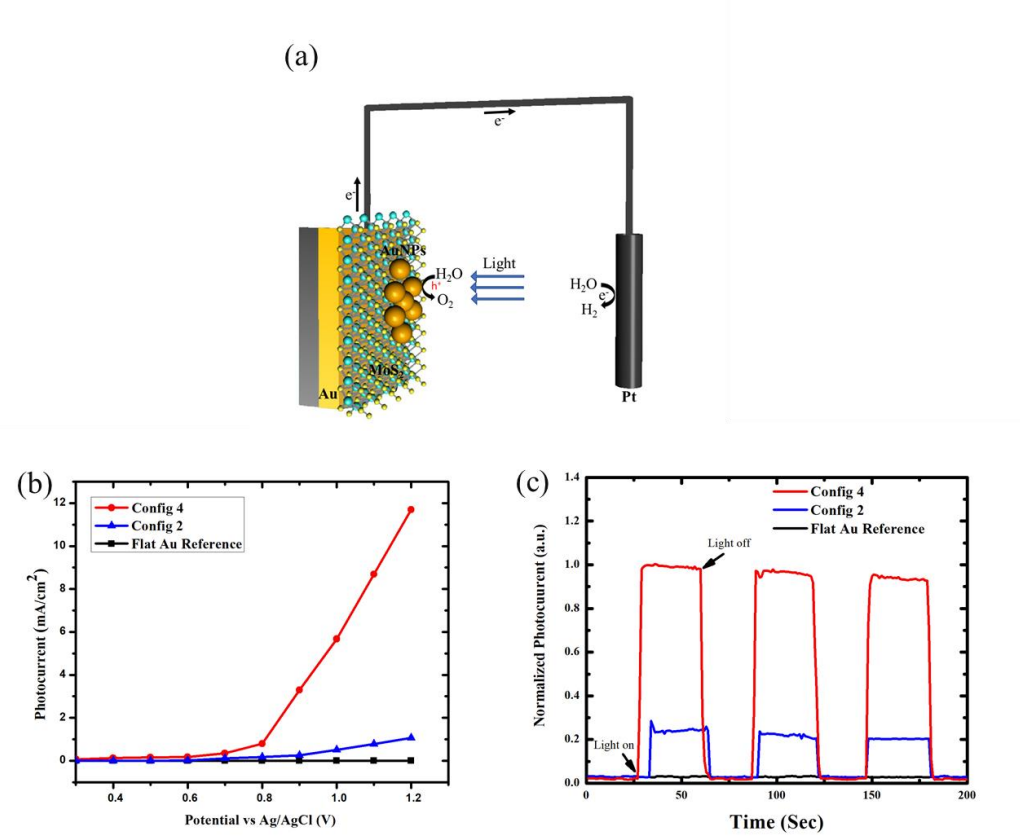


Figure 4. 5 (a) Schematic of $MoS_2$-Au gap plasmon system as photoanode and commercial Pt as photocathode respectively (b) Linear sweep voltammograms for PECs with different working electrodes, config 2 as working electrodes shows in blue, config 4 as working electrodes shows in red. (c) Normalized photocurrent cycles with potential at 0.8 V for PEC with different working electrodes config 2 as working electrodes shows in blue, config 4 as working electrodes shows in red.

## 4.4 Conclusion

In conclusion, single-layer $MoS_2$-Au gap plasmon system with the enhanced photoelectrochemical water-splitting activity is demonstrated for the first time. The use of sub-nanometer thick $MoS_2$ as space layer enables gap plasmonic coupling throughout the $MoS_2$ with the significantly higher field enhanced. A 5-fold increase in photocurrent is achieved through $MoS_2$-Au gap plasmon as the working electrode. With the systematically study, it is revealed that single-layer $MoS_2$-Au gap plasmon system can theoretically generate up to 8 orders of magnitudes SERS EF locally confirmed via FDTD simulation. The $MoS_2$ Raman intensity is tremendously enhanced from the $MoS_2$-Au gap plasmon system, the SERS EF up to $5x10^6$ is obtained, one of the highest values that is ever reported to plasmon-enhanced $MoS_2$ Raman study. Our results provide a plausible solution to enhance the light trapping and photocatalytic response towards the ultrathin $MoS_2$, solving the problem that trade-off the small diffusion length of carrier and the low light absorption.

4.5 Reference

1. Veziroğlu, T. N., Hydrogen movement and the next action: fossil fuels industry and sustainability economics. *International journal of hydrogen energy* 1997, *22* (6), 551-556.

2. O'hayre, R.; Cha, S.-W.; Colella, W.; Prinz, F. B., *Fuel cell fundamentals*. John Wiley & Sons: 2016.

3. Grätzel, M., Photoelectrochemical cells. *nature* 2001, *414* (6861), 338-344.

4. Hisatomi, T.; Kubota, J.; Domen, K., Recent advances in semiconductors for photocatalytic and photoelectrochemical water splitting. *Chemical Society Reviews* 2014, *43* (22), 7520-7535.

5. Roger, I.; Shipman, M. A.; Symes, M. D., Earth-abundant catalysts for electrochemical and photoelectrochemical water splitting. *Nature Reviews Chemistry* 2017, *1* (1), 1-13.

6. Abe, R., Recent progress on photocatalytic and photoelectrochemical water splitting under visible light irradiation. *Journal of Photochemistry and Photobiology C: Photochemistry Reviews* 2010, *11* (4), 179-209.

7. Warren, S. C.; Thimsen, E., Plasmonic solar water splitting. *Energy Environ. Sci.* 2012, *5* (1), 5133-5146.

8. Walter, M. G.; Warren, E. L.; McKone, J. R.; Boettcher, S. W.; Mi, Q.; Santori, E. A.; Lewis, N. S., Solar water splitting cells. *Chemical reviews* 2010, *110* (11), 6446-6473.

9. McKone, J. R.; Lewis, N. S.; Gray, H. B., Will solar-driven water-splitting devices see the light of day? *Chemistry of Materials* 2014, *26* (1), 407-414.

10. Kim, T. W.; Choi, K.-S., Nanoporous BiVO4 photoanodes with dual-layer oxygen evolution catalysts for solar water splitting. *Science* 2014, *343* (6174), 990-994.

11. Mettee, H.; Otvos, J. W.; Calvin, M., Solar induced water splitting with p/n heterotype photochemical diodes: n-Fe2O3/p-GaP. *Solar Energy Materials* 1981, *4* (4), 443-453.

12. Khan, S. U.; Al-Shahry, M.; Ingler, W. B., Efficient photochemical water splitting by a chemically modified n-TiO2. *science* 2002, *297* (5590), 2243-2245.

13. Wang, G.; Wang, H.; Ling, Y.; Tang, Y.; Yang, X.; Fitzmorris, R. C.; Wang, C.; Zhang, J. Z.; Li, Y., Hydrogen-treated TiO2 nanowire arrays for photoelectrochemical water splitting. *Nano letters* 2011, *11* (7), 3026-3033.

14. Ni, M.; Leung, M. K.; Leung, D. Y.; Sumathy, K., A review and recent developments in photocatalytic water-splitting using TiO2 for hydrogen production. *Renewable and Sustainable Energy Reviews* 2007, *11* (3), 401-425.

15. Kondo, J., Cu 2 O as a photocatalyst for overall water splitting under visible light irradiation. *Chemical Communications* 1998, (3), 357-358.

16. Yin, Z.; Chen, B.; Bosman, M.; Cao, X.; Chen, J.; Zheng, B.; Zhang, H., Au nanoparticle-modified MoS2 nanosheet-based photoelectrochemical cells for water splitting. *Small* 2014, *10* (17), 3537-43.

17. Joshi, R.; Shukla, S.; Saxena, S.; Lee, G.-H.; Sahajwalla, V.; Alwarappan, S., Hydrogen generation via photoelectrochemical water splitting using chemically exfoliated MoS2 layers. *AIP Advances* 2016, *6* (1), 015315.

18. Kang, J.; Tongay, S.; Zhou, J.; Li, J.; Wu, J., Band offsets and heterostructures of two-dimensional semiconductors. *Applied Physics Letters* 2013, *102* (1), 012111.

19. Li, A.; Isaacs, S.; Abdulhalim, I.; Li, S., Ultrahigh enhancement of electromagnetic fields by exciting localized with extended surface plasmons. *The Journal of Physical Chemistry C* 2015, *119* (33), 19382-19389.

20. Lee, H. S.; Min, S.-W.; Chang, Y.-G.; Park, M. K.; Nam, T.; Kim, H.; Kim, J. H.; Ryu, S.; Im, S., MoS2 nanosheet phototransistors with thickness-modulated optical energy gap. *Nano letters* 2012, *12* (7), 3695-3700.

21. Joshi, R. K.; Shukla, S.; Saxena, S.; Lee, G. H.; Sahajwalla, V.; Alwarappan, S., Hydrogen generationviaphotoelectrochemical water splitting using chemically exfoliated MoS2layers. *AIP Advances* 2016, *6* (1), 015315.

22. Li, X.; Choy, W. C. H.; Ren, X.; Zhang, D.; Lu, H., Highly Intensified Surface Enhanced Raman Scattering by Using Monolayer Graphene as the Nanospacer of Metal Film-Metal Nanoparticle Coupling System. *Advanced Functional Materials* 2014, *24* (21), 3114-3122.

23. Ye, P.; Xin, W.; Zheng, L.; Xie, Y.-H., Uniform growth of high-concentration MoS2 nanoflakes on plasma treated carbon nanotube sheet. *Materials Letters* 2019, *256*, 126665.

24. Xin, W.; De Rosa, I. M.; Ye, P.; Severino, J.; Li, C.; Yin, X.; Goorsky, M. S.; Carlson, L.; Yang, J. M., Graphene template-induced growth of single-crystalline gold nanobelts with high structural tunability. *Nanoscale* 2018, *10* (6), 2764-2773.

25. Li, H.; Wu, J.; Huang, X.; Yin, Z.; Liu, J.; Zhang, H., A universal, rapid method for clean transfer of nanostructures onto various substrates. *ACS nano* 2014, *8* (7), 6563-6570.

26. Johnson, P. B.; Christy, R.-W., Optical constants of the noble metals. *Physical review B* 1972, *6* (12), 4370.

27. Laturia, A.; Van de Put, M. L.; Vandenberghe, W. G., Dielectric properties of hexagonal boron nitride and transition metal dichalcogenides: from monolayer to bulk. *npj 2D Materials and Applications* 2018, *2* (1), 1-7.

28. Tanaka, K.; Tanaka, M., Simulations of nanometric optical circuits based on surface plasmon polariton gap waveguide. *Applied Physics Letters* 2003, *82* (8), 1158-1160.

29. Gnedenko, O. V.; Mezentsev, Y. V.; Molnar, A. A.; Lisitsa, A. V.; Ivanov, A. S.; Archakov, A. I., Highly sensitive detection of human cardiac myoglobin using a reverse sandwich immunoassay with a gold nanoparticle-enhanced surface plasmon resonance biosensor. *Analytica chimica acta* 2013, *759*, 105-109.

30. Cristol, S.; Paul, J.; Payen, E.; Bougeard, D.; Clémendot, S.; Hutschka, F., Theoretical study of the MoS2 (100) surface: a chemical potential analysis of sulfur and hydrogen coverage. *The Journal of Physical Chemistry B* 2000, *104* (47), 11220-11229.

31. Li, H.; Zhang, Q.; Yap, C. C. R.; Tay, B. K.; Edwin, T. H. T.; Olivier, A.; Baillargeat, D., From bulk to monolayer MoS2: evolution of Raman scattering. *Advanced Functional Materials* 2012, *22* (7), 1385-1390.

32. Narayana, S.; Sato, Y., DC magnetic cloak. *Advanced Materials* 2012, *24* (1), 71-74.

33. Wang, P.; Zhang, W.; Liang, O.; Pantoja, M.; Katzer, J.; Schroeder, T.; Xie, Y.-H., Giant optical response from graphene–plasmonic system. *Acs Nano* 2012, *6* (7), 6244-6249.

34. Mock, J. J.; Hill, R. T.; Tsai, Y.-J.; Chilkoti, A.; Smith, D. R., Probing dynamically tunable localized surface plasmon resonances of film-coupled nanoparticles by evanescent wave excitation. *Nano letters* 2012, *12* (4), 1757-1764.

35. Xia, M.; Li, B.; Yin, K.; Capellini, G.; Niu, G.; Gong, Y.; Zhou, W.; Ajayan, P. M.; Xie, Y.-H., Spectroscopic signatures of AA′ and AB stacking of chemical vapor deposited bilayer MoS2. *ACS nano* 2015, *9* (12), 12246-12254.

36. Shen, Y.; Miao, P.; Hu, C.; Wu, J.; Gao, M.; Xu, P., SERS-Based Plasmon-Driven Reaction and Molecule Detection on a Single Ag@ MoS2 Microsphere: Effect of Thickness and Crystallinity of MoS2. *ChemCatChem* 2018, *10* (16), 3520-3525.

37. Su, S.; Zhang, C.; Yuwen, L.; Chao, J.; Zuo, X.; Liu, X.; Song, C.; Fan, C.; Wang, L., Creating SERS hot spots on MoS2 nanosheets with in situ grown gold nanoparticles. *ACS applied materials & interfaces* 2014, *6* (21), 18735-18741.

38. Yin, Z.; Chen, B.; Bosman, M.; Cao, X.; Chen, J.; Zheng, B.; Zhang, H., Au nanoparticle-modified MoS2 nanosheet-based photoelectrochemical cells for water splitting. *Small* 2014, *10* (17), 3537-3543.

39. Brassard, J.-D.; Sarkar, D. K.; Perron, J., Synthesis of monodisperse fluorinated silica nanoparticles and their superhydrophobic thin films. *ACS applied materials & interfaces* 2011, *3* (9), 3583-3588.

40. Subramanian, V.; Wolf, E. E.; Kamat, P. V., Catalysis with TiO2/gold nanocomposites. Effect of metal particle size on the Fermi level equilibration. *Journal of the American Chemical Society* 2004, *126* (15), 4943-4950.

41. Murdoch, M.; Waterhouse, G.; Nadeem, M.; Metson, J.; Keane, M.; Howe, R.; Llorca, J.; Idriss, H., The effect of gold loading and particle size on photocatalytic hydrogen

production from ethanol over Au/TiO 2 nanoparticles. *Nature chemistry* 2011, *3* (6), 489-492.

42. Wang, M.; Chen, L.; Sun, L., Energy Environ. Sci., 2012, 5, 6763;(e) VS Thoi, Y. Sun, JR Long and CJ Chang. *Chem. Soc. Rev* 2013, *42*, 2388.

4.6 Supplementary Information

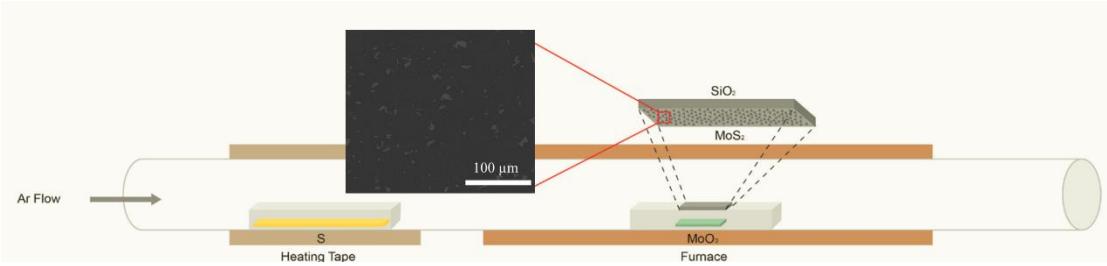


Figure S4. 1 Schematic illustration of chemical vapor deposition method for $MoS_2$ grow on $SiO_2$ substrate. Inset SEM image shows the nearly continuous monolayer $MoS_2$ (up to 90% coverage)

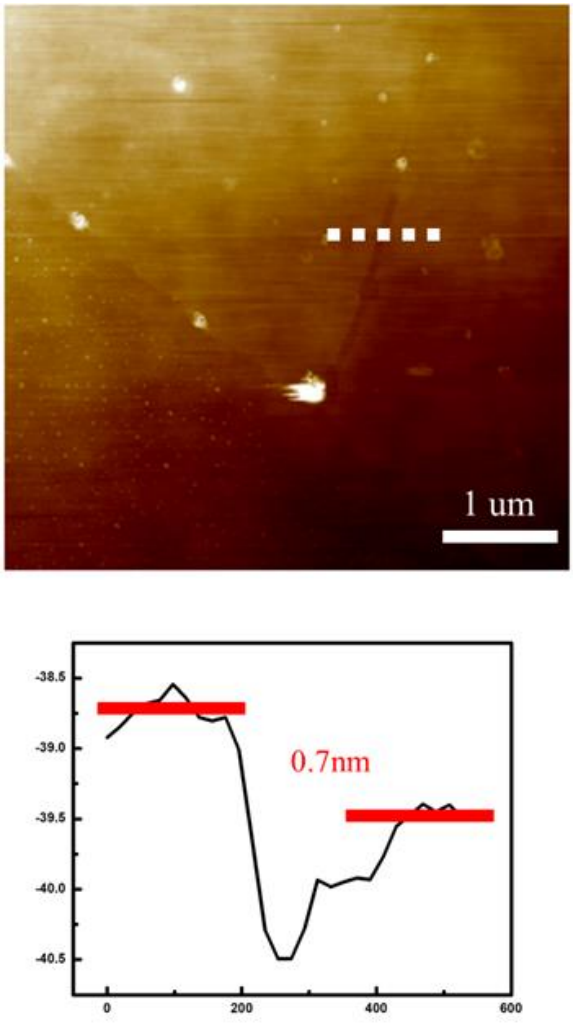


Figure S4. 2 AFM image of the obtained from CVD growth $MoS_2$ samples on $Si/SiO_2$ substrate. The height profile obtains from the edge $MoS_2$ crystal. The height measured 0.7nm corresponds with the monolayer $MoS_2$ profiles.

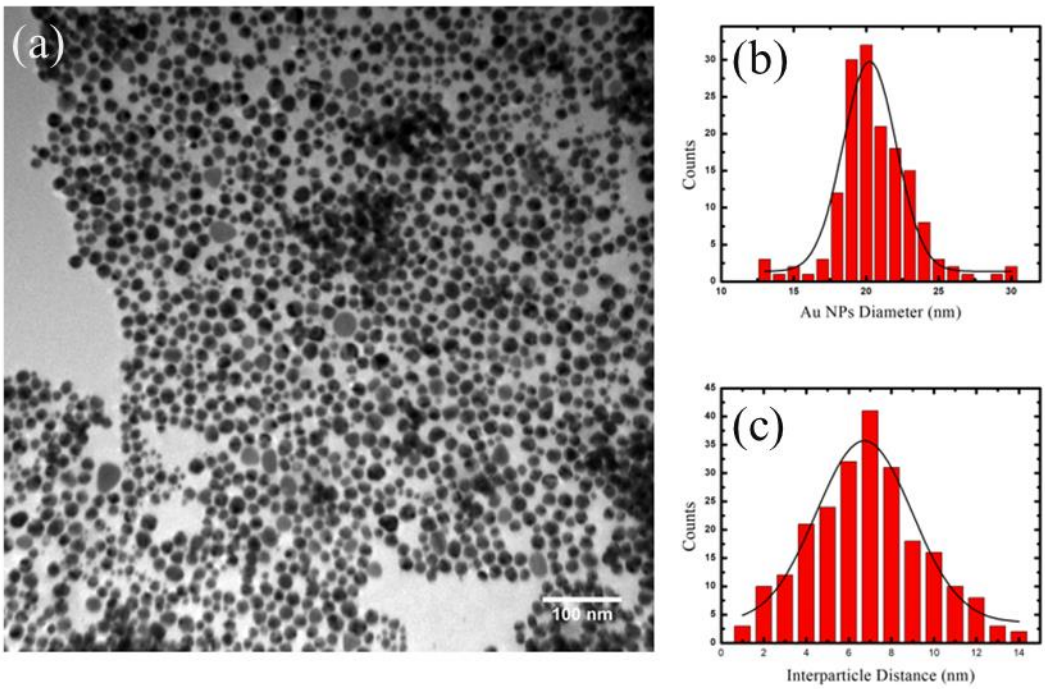


Figure S4. 3 (a)high-resolution TEM image of as-fabricated AuNPs deposited on TEM grids. (b) AuNPs diameter distribution histogram, (c) AuNPs interparticle distance distribution histogram.

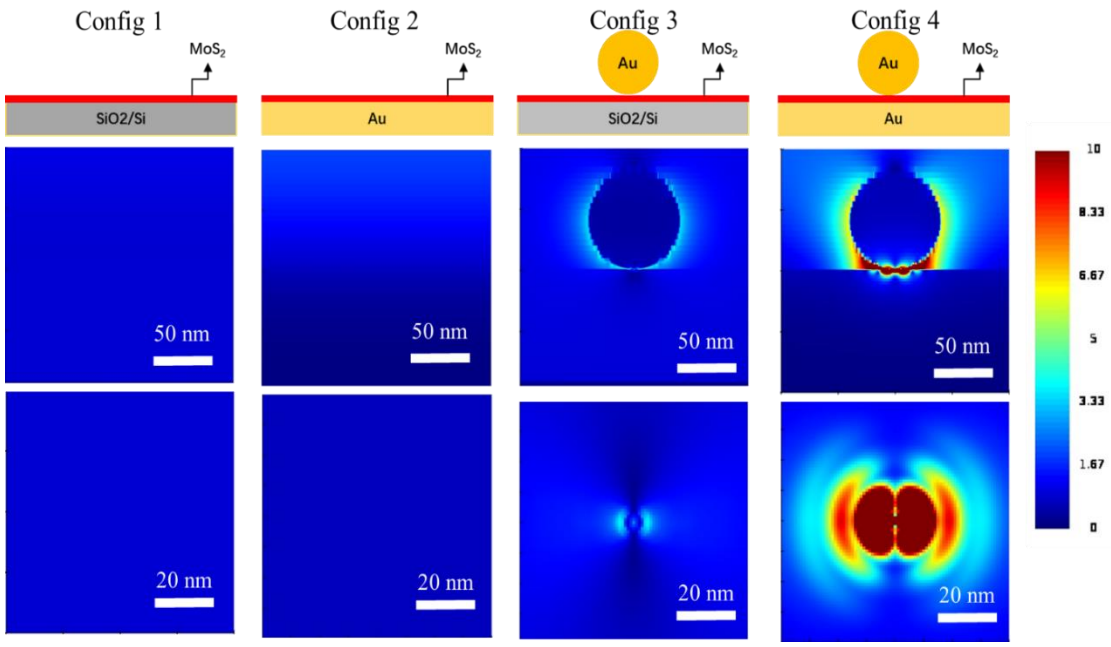


Figure S4. 4 Electrical Field enhancement ($E/E_0$) distribution side view and top view from 4 different configurations

# Chapter 5 Conclusions and Future Work

## 5.1 Conclusions

This dissertation demonstrated the feasibility of the gap plasmon enhanced monolayer $MoS_2$ based efficient and sustainable photocatalytic water splitting platform. The following is a summary of the dissertation work presented:

In Chapter 2, we introduce a novel strategy of growing $MoS_2$ nanoflakes on CNT sheet that shows significance in the following two aspects: first, the direct growth of large quantity $MoS_2$ nanoflakes on carbon nanotube sheet is realized. To the best of our knowledge, this is the first time to grow large quantities $MoS_2$ nanoflakes directly on the substrate of the CNT sheet. Second, plasma-activated CNT sheet is of critical importance to immobilize $MoS_2$ nanoflakes. We reveal that plasma treatment of the CNT sheet results in de-bundling and activation of carbon nanotube bundles, which promotes the deposition of $MoS_2$ nanoflakes.

In Chapter 3, we present a novel way to synthesis Au nanoframes, which have been shown to possess distinguished plasmonic properties comparing to other metal nanocrystal geometry. However, current approaches to obtain these nanoframes usually involve multi-step treatment. In this work, we demonstrate a facile one-step growth-etching approach of self-templated hollow Au nanoframes, which shows significant merits in the following aspects: First, A facile one-step route to synthesize Au nanoframes based on the etching of self-templates is realized for the first time. High-quality Au nanoplates with tunable thickness are first synthesized, from which Au nanoframes can be evolved with enough etching time. We find a synergistic effect from $Ag^+$ and $Br^-$ ions as the key factors to the

formation of predominantly Au nanoframes. Second, the dispersion issue of Au nanoframes is significantly improved using graphene as a template. The improved dispersion is attributed to the presence of anchoring sites on graphene, which could immobilize Au nanocrystals from the nucleation stage and make the ultimate dispersion more homogenous. Third. Graphene/Au nanoframe hybrid platform shows great potential in surface enhanced Raman spectroscopy (SERS) that is highly relevant to the application such as biosensing. The hybrid platform is capable of rendering single molecule sensitivity proven via both simulation and experiment results.

In Chapter 4, we present using single-layer $MoS_2$ as the space layer inside gap-plasmon system to achieved enhanced photoelectrochemical water splitting. The enhancement in this work is due to plasmon resonances between AuNPs and Au films. A 5-fold increase in the photocurrent was achieved across $MoS_2$-Au gap plasmon working electrode. With the systematic study, we reveal that $MoS_2$-Au gap plasmon system can theoretically increase nearly 8 orders of magnitude's enhancement factor via FDTD simulation. The $MoS_2$ Raman intensity is tremendously enhanced from the $MoS_2$-Au gap plasmon system, the SERS EF up to $5x10^6$ is obtained, one of the highest values that is ever reported to plasmon-enhanced $MoS_2$ Raman study. Our results provide a plausible solution to enhance the light trapping and photocatalytic response towards the ultrathin $MoS_2$, solving the problem that trade-off the small diffusion length of carrier and the low light absorption.

## 5.2 Future Work

For the platform to be sustainable in nature as well as the broadband resonance within the visible light region, replacing precious metal Au employed for the plasmonic substrate with other more environmentally rich elements like Ag, Cu, Al is investigated. The preliminary study using FDTD modeling of replacing bottom Au film with sustainable Ag, Cu, Al is simulated shown in figure 5.1, the reason we only replace the bottom film instead of the AuNPs is that the Ag, Cu, Al is not corrosion-resistant, by placing metal under continuous $MoS_2$ film, $MoS_2$ as a well-known diffusion barrier can prevent $O_2$ penetrate through to corrode metal film underneath[1].

It is observed that AuNPs and Au films coupling only resonance while incident wavelength at 650 nm and 596 nm, significantly less hot spot and hot spot density are observed while further decrease the incident wavelength in the simulation result in figure 5.1 row one. The result corresponds with the quality value of Au shown in figure 1.4. It is observed that Cu films show strong resonance with AuNPs not only at 650 nm and 596 nm as well as at 513 nm, which means Cu have broader band resonance with AuNPs, however, further decrease incident wavelength to 450 nm, the resonance also decrease dramatically observed from simulation results in row two. When using Al or Ag as bottom metal film in gap plasmon system, we find strong resonance on all four wavelengths that was simulated. Strong hot spots and high hot spots density can be clearly observed under 450 nm wavelength shown in figure 5.1

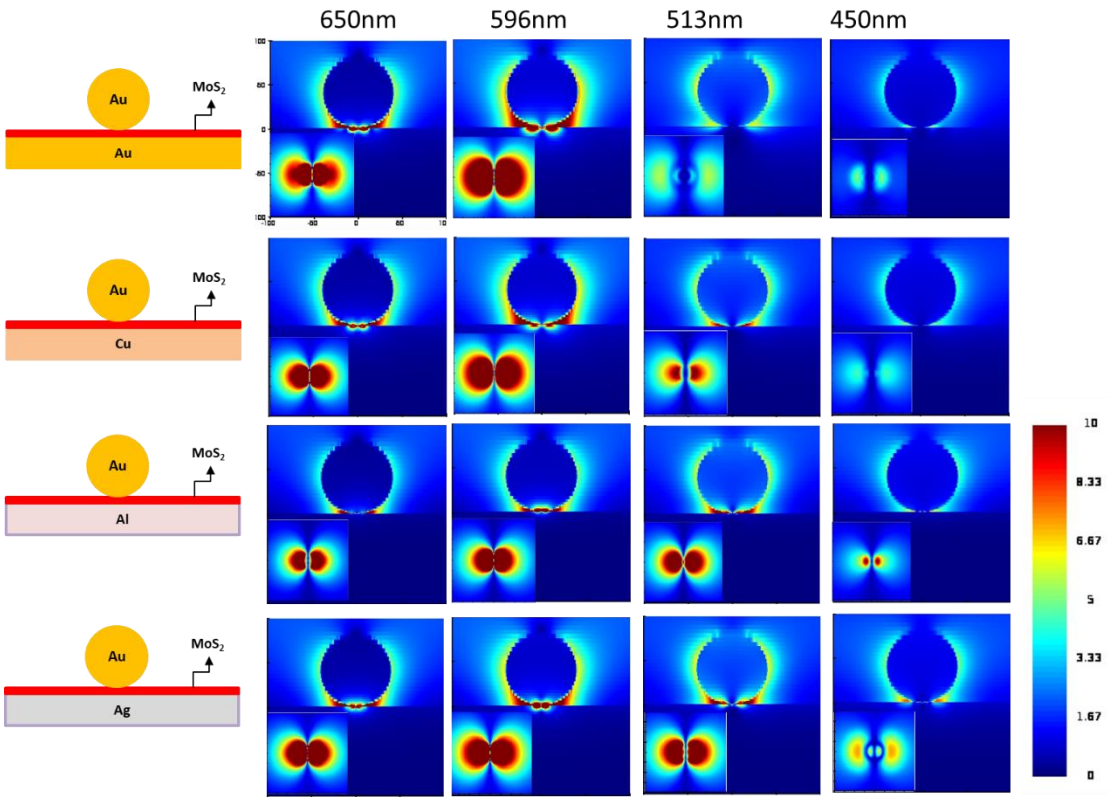


Figure 5. 1 EM field distributions for the AuNP coupling with various metal films separated by a 1 nm $MoS_2$ spacer at 450 nm, 513 nm, 596nm and 785 nm, respectively.

In order to better compare which metal film resonate with AuNPs more efficiently, we need to consider both hot spot and hot spot density, here the quality factor is defined as equation below

$$Q = \iint_{x,y=-40}^{x,y=40} E^2 dxdy$$

This self-defined quality factor represents the total stored energy of the resonator along the surface of the $MoS_2$ under the cross-section area of the Au nanoparticles to by considering both hot spot and hot spot density, the data is extracted from simulation results.

Q value comparison with different metal under different wavelength is obtained in figure 5.2. From the plot we can draw the conclusion that Ag film can store the most available light energy from 450nm to 650nm, which proves Ag film resonates more with AuNPs in a broader band resonance between 450nm to 650nm. This finding corresponds with figure 1.4 that Ag shows the highest Q factor from 400nm and up.

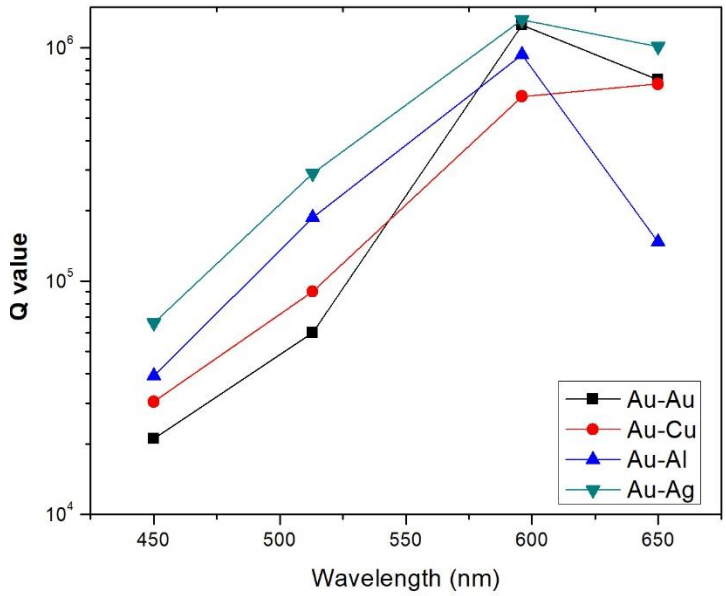


Figure 5. 2 Quality factor as a function of wavelength for different metal films and AuNPs coupling.

However, the substitution may bring the potential problem of Ag corrosion. Here, $MoS_2$ has already been proven to be a very effective diffusion barrier for $O_2$ penetration, the strong sulfur-oxygen interaction makes it difficult for oxygen molecule to penetrate through even for single-layer $MoS_2$, the diffusion energy barrier for $O_2$ molecular to penetrate through is calculated to be 13.94 eV[1], this diffusion energy barrier is significantly larger than the reported barrier for suspended graphene (5.98 eV) which is widely known

as a good corrosion protective barrier[1-3]. Ag plasmonic substrate will be completely protected if we have continuously monolayer $MoS_2$ covered on top to prevent potential corrosion or oxidation. This event may raise another potential issue that is a method to fabricate continuously exclusive single-layer $MoS_2$, current growth recipe can hardly control for the perfect exclusive continuous single-layer $MoS_2$ growth, the typical result is either near continuously single-layer $MoS_2$ film or sometimes slightly more than one single-layer $MoS_2$, it is relative hard to control the perfect timing to grow exact the 100% coverage single-layer $MoS_2$. We will address this issue by first over-grow $MoS_2$ to be slightly more than one single layer. We propose to use an energy-band gap dependent, self-limiting etching process for produce exact single layer $MoS_2$. A selective photo-activated etching recipe need to be developed. The physics basis for the selective photo-activation is the narrower $E_g$ of multiple layer $MoS_2$ compared to that of single layer $MoS_2$. By employing an etchant that can barely etches $MoS_2$ in the absence of light, we expect that illuminating the surface of MoS2 with patches of different thickness as obtained from typical chemical vapor deposition (CVD) growths[4] using photons with energy precisely controlled to be just below the $E_g$ of single layer $MoS_2$ could provide the etch rate differential needed to obtain single layer $MoS_2$ covering the entire substrate surface.

5.3 References

1. Sen, H. S.; Sahin, H.; Peeters, F.; Durgun, E., Monolayers of MoS2 as an oxidation protective nanocoating material. *Journal of Applied Physics* 2014, *116* (8), 083508.

2. Kirkland, N.; Schiller, T.; Medhekar, N.; Birbilis, N., Exploring graphene as a corrosion protection barrier. *Corrosion Science* 2012, *56*, 1-4.

3. Zhang, X.; Yan, X.; Chen, J.; Zhao, J., Large-size graphene microsheets as a protective layer for transparent conductive silver nanowire film heaters. *Carbon* 2014, *69*, 437-443.

4. Lee, Y. H.; Zhang, X. Q.; Zhang, W.; Chang, M. T.; Lin, C. T.; Chang, K. D.; Yu, Y. C.; Wang, J. T. W.; Chang, C. S.; Li, L. J., Synthesis of Large-Area MoS2 Atomic Layers with Chemical Vapor Deposition. *Advanced Materials* 2012, *24* (17), 2320-2325.